Evaluation of fracture toughness for CFRP joints with highly toughened epoxy adhesive under mixed-mode (mode I + II) condition and plastic behavior of epoxy adhesive for various stress multiaxialities

（高じん性エポキシ接着剤による CFRP 接着継手の混合モード（モードⅠ+Ⅱ）状態における破壊じん性の評価と種々の応力多軸度におけるエポキシ接着剤の塑性挙動の研究）

July, 2024

Yousuke Kouno

Mechanical Engineering Program
Graduate School of Advanced Science and Engineering,
Hiroshima University

Contents

Chapter 1 Background and objective

1.1 Introduction and Background

In the last decades, light-weight materials such as fiber reinforced plastics (FRP) and aluminum alloy have been widely used to reduce fuel consumption as well as weight reduction. The combination of FRP and metallic materials is also attracting attention as multi-material design or hybrid design. Adhesive bonding is considered the most promising method for joining FRP to FRP or FRP to metallic materials. Therefore, there has been growing interest in adhesively bonding in a wide range of industries, including the automotive, maritime and space industries. Adhesive bonding plays an important role in integrating individual parts and transferring loads. In the design of mechanical structures, it is becoming more important to ensure the safety of integrated structure as well as individual parts. Structural analysis using the finite element method (FEM) has become popular as a simulation tool to solve these problems and contribute to design works.

There are many factors that must be considered in the design of adhesive joints, including stress concentration, interfacial strength between adherend and adhesive, manufacturing defects, fatigue loading, mixed mode loading, and many others, in order to more accurately predict their strength. The stress field near the bonding edge is known to exhibit the singularity behavior [1-2]. An example of the stress distribution in the adhesive layer for single-lap adhesive joint determined by using theoretical stress analysis method [3] is shown in Fig. 1.1. The single-lap joint is a typical adhesive joint in practical use, in which thickness changes in a step-like manner at the overlap. The thin adhesive layer located at the center of the sandwich structure between two adherends is subjected to high shear stress condition. In addition, the joint is also subjected to moment due to the mismatch of the loading axes of the two adherends. Because of these structural features, the adhesive layer has been subjected to shear stress and tensile stress simultaneously, and both of them exhibit the singularity behavior. It can be seen that shear stress τ_{xy} and peel stress σ_y are sharply higher at the edges where $X/L = 1.0, -1.0$ as shown in Fig. 1.1. Therefore, even in the case of uniaxial loading, it is necessary to evaluate the strength of adhesive joints by considering both shear stress and tensile stress and their singularities.

As can be seen from the above, in adhesive joints, it is important to correctly evaluate the stress at the ends and corners where stress concentration occurs. Because the adhesive is located in thin layers compared to other adherends, its mesh size must be sufficiently fine when using FEM to accurately predict such stress distributions in the adhesive. However, it is not reasonable method to obtain accurate stress in the adhesive using finite element (FE) simulation with fine mesh, because it results in large volume of analysis

data and extremely high computational cost. Therefore, it is necessary to establish a simple and accurate analysis method for evaluating the strength of adhesive joints instead of computationally heavy FE simulation.

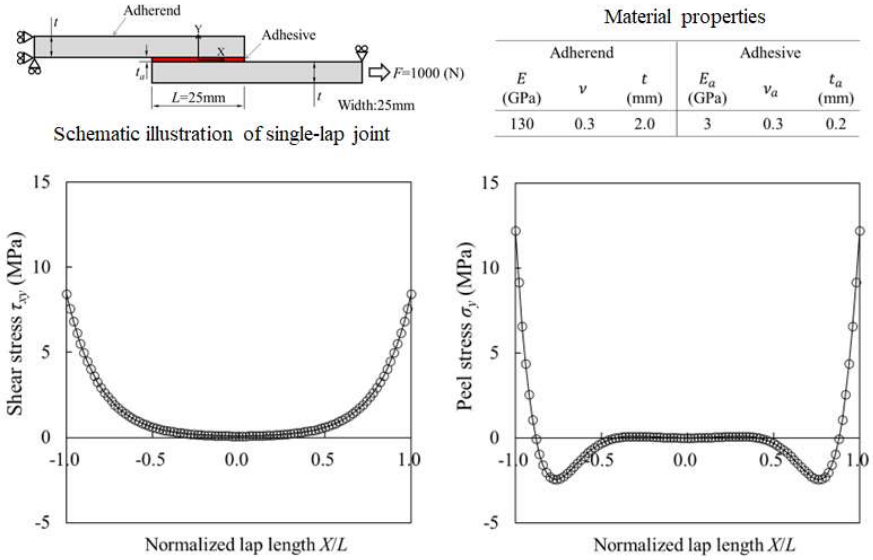

Fig. 1.1 Stress distribution example in the adhesive for single lap adhesive joint obtained by Goland-Reissner analysis [3].

On the other hand, the method predicting the strength of adhesively joints based on fracture mechanics has contributed to the evaluation of fracture phenomena of adhesive joints. In fracture mechanics, it has been assumed that local damage inside the adhesive has become to crack that propagate in the adhesive layer. For FE analysis based on fracture mechanics, a method using cohesive zone modeling (CZM) based on energy release rate was proposed. In numerical analysis, CZM can describe the failure process as the formation of the cohesive zone, initiation of damage, softening of tractions and completely separation of materials, by using the traction-separation law. Other methods for analyzing crack initiation or propagation include the extended finite element method (XFEM) and continuum damage models. These methods are effective for evaluating crack propagation in adhesive, but the computational cost is higher than CZM. Therefore, assuming that cracks propagate along the adhesive layer in the adhesively bonded joints, inserting the CZM elements into the adhesive layer is considered to be one of the most effective methods for evaluating adhesive strength. CZM requires the fracture toughness to define the traction-separation law. The fracture toughness corresponds to the area

enclosed by the curve of the traction-separation law, and it plays an important role in determining complete material failure.

In designing adhesive joints, brittle failure has been an important issue to be avoided. Toughened epoxy adhesives were developed to prevent such brittle failure, and their fracture toughness values are several times greater than those of conventional adhesives. In general, toughened epoxy adhesive exhibits a tendency for the energy release rate to increase with crack propagation as shown by so-called *R*-curve in Fig. 1.2 [4]. On the other hand, conventional epoxy resin does not exhibit *R*-curve, and crack propagates unstably. Therefore, in order to evaluate joint strength of the toughened epoxy adhesive using CZM, it is important to obtain the *R*-curve of the toughened epoxy adhesive and evaluate its fracture toughness.

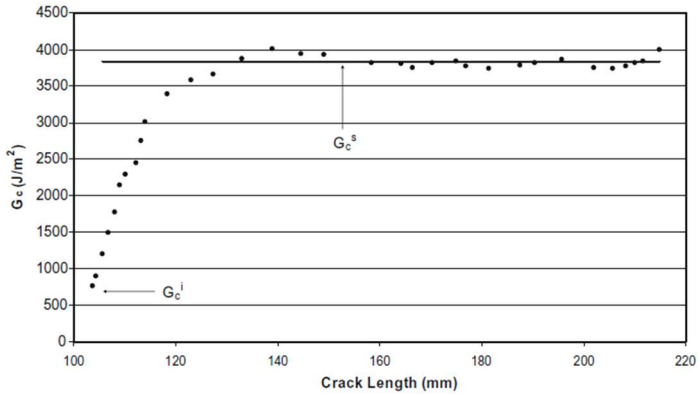

Fig. 1.2 Typical *R*-curve behavior of a double cantilever beam (DCB) joint under the mixed-mode condition [4].

The high fracture toughness value of the toughened epoxy adhesive described above has been achieved by adding micro rubber particles into the resin. Rubber particles have lower modulus of elasticity and deformation resistance compared to epoxy resin. In multiaxial stress field, these particles would cause cavitation failure by tensile stress as shown in Fig. 1.3 [5]. The black area in Fig. 1.3 (b) shows cavitation fracture. In uniaxial tensile stress or pure shear stress conditions, the effect of cavitation is expected to be small. However, the fracture mechanism of adhesive is expected to be different in multiaxial stress field compared to uniaxial stress field. Therefore, yield criterion of the toughened epoxy adhesive should be defined appropriately to account for the effects of the stress field. In other words, yield criterion for the toughened epoxy adhesive should be defined in a manner that includes the effect of stress multiaxiality (or hydrostatic stress).

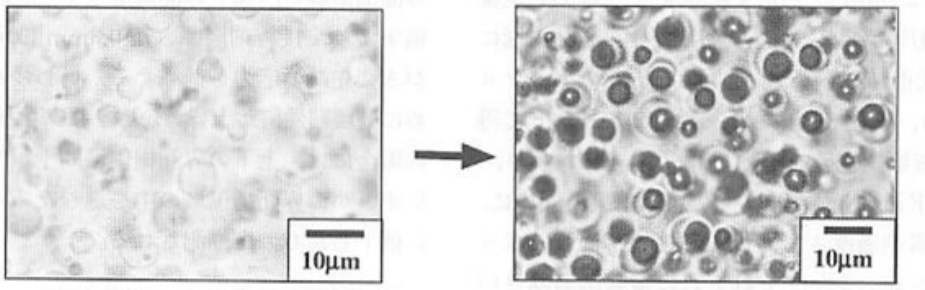

(a) Virgin (b) Damaged

Fig. 1.3 Cavitation of damaged rubber particles [5].

As described above, there are a number of issues that need to be studied in the design of adhesive joints (particularly toughened epoxy adhesive joints). This study specifically focused on the toughened epoxy adhesive and investigated the fracture toughness under mixed-mode conditions, crack propagation analysis using FE models with CZM, and yielding behavior of adhesive joint in multiaxial stress field.

1.2 Literature Survey

This chapter contains discussions on the previous studies on mixed-mode fracture toughness in adhesively bonded joints, failure predictions of adhesively bonded joints and yield criteria of ductile adhesive.

1.2.1 Mixed-mode fracture toughness test

In recent years much effort has been devoted to the fracture toughness characterization of adhesive bonded joints. In order to determine their fracture toughness, many experimental methods have been proposed. With regard to the mixed-mode (mode I + mode II), the mixed-mode bending (MMB) is commonly used for the characterization of the fracture behavior of adhesively bonded joints.

To ensure the strength of the adhesively bonded joints, ductile adhesive have been widely employed. Since ductile adhesive is known to exhibit elastic-plastic behavior and cracks propagate in the adhesive layer with stability, it is necessary to evaluate the relationship between fracture toughness and crack length during crack propagation (*R*-curve, see Fig. 1.2).

Several authors have presented mixed-mode fracture toughness for adhesively bonded joints using MMB [6, 7]. Due to the difficulty in having a sufficient distance between crack tip and loading device, the evaluation of *R*-curve has been limited to crack

length up to about 15 mm. It is necessary to select a suitable method in which the crack tip is less sensitive to test jig, in order to accurately evaluate the crack propagation behavior during test. One of the appropriate apparatuses is Fernlund and Spelt jig [8]. This jig has the advantage of a longer ligament section and is particularly suitable for the evaluation of R-curve properties because the crack tip is located far enough from the loading device. Several studies exist that have evaluated R-curves of mixed-mode fracture toughness using Fernlund and Spelt jig [4, 9-10]. However, to the best of the author's knowledge, there are no studies that quantitatively evaluate the R-curve of toughened adhesive under a wide range of mixed-mode conditions ($0 \leq G_{II}/G_T \leq 0.8$) using Fernlund and Spelt jig. Here $G_T = G_I + G_{II}$, G_I and G_{II} are energy release rates in modes I and II, respectively, and G_{II}/G_T is mode ratio.

1.2.2 Cohesive zone modeling

Cohesive element can be treated as one of the interface elements which is acting between the continuum elements. It has following three characteristics.

1) It has no Young's modulus and Poisson's ratio.
2) Nonlinear behavior of CZM is controlled by the relationship between traction and separation (i.e. traction-separation law).
3) It allows zero thickness.

Essentially, CZM has been widely used to evaluate the delamination of carbon fiber reinforced plastics (CFRP) and the interfacial strength between fibers and matrix resin. In recent years, CZM is widely used for design of adhesive joints because it is capable of evaluating crack propagation. Failure criterion of CZM is influenced by the relationship between traction and separation (traction-separation law). The traction-separation law plays an important role in the behavior of the CZM from damage initiation to dissipation of its energy. Various traction-separation relationships have been proposed. Typical traction-separation laws that have been proposed are known such as bilinear, exponential-linear, and trapezoidal models as schematically shown in Fig. 1.4.

The bilinear model is the most basic traction-separation law and has been employed in many studies. In terms of its simple triangular shape, it has the advantage of being able to be defined with fewer parameters. The bilinear model is often applied to brittle materials such as epoxy adhesives [11-14]. Several studies have been conducted on the applicability of exponential-linear model [15-17]. Compared to the bilinear model, the exponential linear model can deal with toughened materials because the area enclosed by the traction-separation curve (i.e. the fracture energy) ensure larger. The trapezoidal

model has been employed to adhesive joints with ductile adhesives [18-21]. Failure criterion of CZM under mixed-mode conditions is defined by the traction-separation law in each mode together with some kind of mixed-mode failure criterion. Several studies defined CZM failure criterion under mixed-mode conditions by using the trapezoidal model together with linear failure criterion [18-19, 21]. In addition to the linear failure criterion, B-K criterion [22-25] and power-law criterion [26] have also been proposed for CZM in mixed-mode conditions, so the applicability of these criteria to the toughened epoxy adhesive joint under mixed-mode loadings should be discussed. In terms of simplicity of the formula, the power-law criterion has the advantage of being easy to use and providing an opportunity for widespread in many industries. However, to the best of the author's knowledge, previous studies that have evaluated load-displacement curves under the mixed-mode conditions using Spelt's jig have used the linear fracture criterion but never employed the power-law failure criterion based on the trapezoidal traction-separation law.

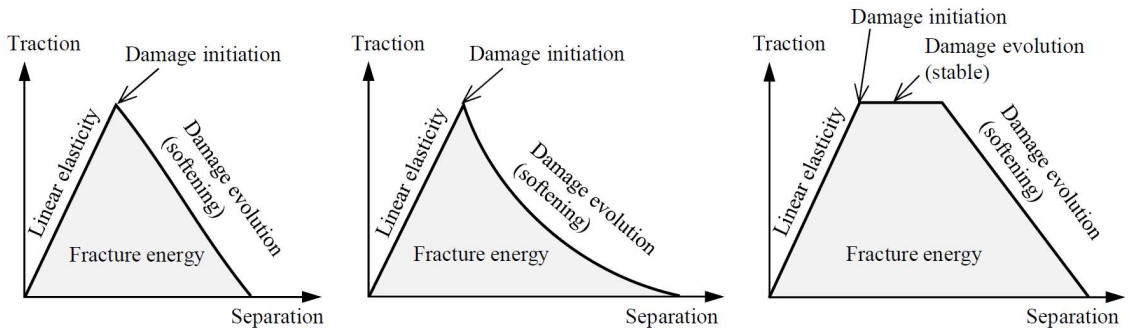

(a) Bilinear model (b) Exponential-linear model (c) Trapezoidal model

Fig. 1.4 Schematics of typical traction-separation laws.

1.2.3 Plasticity modeling of adhesive

It has been reported that the strength of toughened epoxy adhesive is affected by triaxial tensile stress [27, 28]. As previously described, it is known that toughened epoxy adhesive has improved its toughness by adding rubber particles into resign. Bagheri et al. observed rubber particles using scanning electron microscope (SEM) and reported that their diameters to be 0.2 μm~0.7 μm [29]. Imanaka et al. reported that the addition of rubber particles (mean diameter of 70 nm) to epoxy adhesives improved mode I fracture toughness over ten times compared to unmodified adhesive [30].

It has been reported that rubber particles added to adhesive cavitate under triaxial tensile stress, causing crack propagation. Kinloch et al. has suggested that the micro-voids

are produced during ductile stable crack growth by cavitation in the rubbery particles, or debonding at the particle/matrix interface by using compact tension specimens and SEM observations of fracture surfaces formed by stable crack propagation [31]. Scanning electron microscopy of fracture surfaces has indicated that cavitation of the rubber particles is the major deformation mechanism during crack growth, according to Pearson et al. [32]. As can be seen from the above findings, in order to describe yielding behavior for toughened adhesive which includes rubber particles, the consideration of hydrostatic stress is essential.

The stress analyses for the adhesive joints have been carried out using von Mises yield criterion which is commonly employed in metallic materials. However, von Mises yield criterion is not sufficient to reproduce the yielding behavior of toughened epoxy adhesive, because this criterion does not take into account the effects of hydrostatic stress. One yield criterion that can express the effect of hydrostatic stress on yielding behavior is Drucker-Prager model [33-36].

In the exponential Drucker-Prager yield criterion, the influence of hydrostatic stress can be set by the hydrostatic-stress sensitivity parameter λ. Dean et al. reported that the parameter λ identified from the experimental results of bulk adhesive tensile tests and notched plate shear tests can be used to evaluate the stress-strain relationship of another adhesive joint such as butt joint [36]. However, it would be reasonable to define the hydrostatic stress dependence considering the stress state of adhesive layer, since the stress multiaxiality depends on the type of adhesive joint. To the best of the author's knowledge, no study has been reported that investigates the appropriate hydrostatic-stress sensitivity parameter λ, taking into account a wide range of stress multiaxiality in adhesive layers. This is another important issue that motivated this study.

1.3 Objective and outline of this thesis

Joints between composites, and multi-material joints between metals and composite materials are increasingly being developed in many industries. In response to this situation, high-strength adhesives are required to safely maintain the strength of the bonded structure. In general, for the same type of adhesive materials, it is known that high strength adhesives usually fail by brittle fracture process. Therefore, it is necessary to design adhesive joints considering the balance between static strength and fracture toughness. The fracture toughness of adhesive joints is often evaluated in terms of Mode I and Mode II conditions. However, practical adhesive joints are rarely used only in uniaxial loading condition, so they must be evaluated in mixed-mode conditions.

Recently, rubber-modified epoxy adhesive that improve fracture toughness while

maintaining static strength have been developed and widely applied to many structures. This type of adhesive shows a ductile fracture rather than brittle one of conventional epoxy adhesive in failure, resulting in higher fracture energy. Therefore, it is important to measure the relationship between crack length and energy release rate to evaluate strength characteristic against crack.

Traditionally, strength characteristics of adhesive joints have been implemented through experimental trial and error. However, the above approach does not work well in the situation where model-based development (MBD) is focused on in R&D process. Therefore, it is necessary to develop a system that can explain the strength of adhesive joints through simulation. In adhesive joints, stress concentration occurs at the edges, causing crack initiation and propagation which splits the adhesive layer and leads to failure. Considering this fracture process due to crack propagation, the strength of the adhesive bonded joint can be predicted by the CMZ embedded in the FE model. The fracture toughness of the toughened adhesive is given in the *R*-curve, and its energy release rate increases with crack length. For this reason, this study was conducted to investigate whether the crack growth could be predicted by the CZM considering the *R*-curve.

In toughened adhesive joints, the effect of plastic deformation at the crack tip on fracture toughness should be considered. Cavitation failure of micro rubber particles dispersed in the matrix resin affects the yield behavior of the adhesive. To account for cavitation of rubber particles, it is necessary to apply a yield criterion that allows influence of hydrostatic stress. In this study, some yield criteria that can be used to simulate the yielding and plastic behavior of toughened epoxy adhesives under various hydrostatic stress were investigated.

The main structure of this thesis is shown below. Here in Chapter 1, background of this study, survey of the relevant literatures, objective and structure of this thesis are explained. In Chapter 2, the fracture toughness values of adhesive joints were measured under mixed-mode condition. To obtain the *R*-curves, a special loading system which was proposed by Fernlund and Spelt [8] was used. The *R*-curves under the various mixed mode conditions were verified by comparing them with *J*-integral analysis results.

Chapter 3 describes the FE analysis of crack propagation using CZM. The traction-separation law was defined by using *R*-curves which was obtained in Chapter 2. The peak loads in mixed-mode fracture toughness tests were estimated by CZM. The accuracy of the prediction was verified by two types of energy-based failure criteria i.e. linear criterion and power-law criterion.

In Chapter 4, yield criterion and plastic behavior of toughened epoxy adhesive joints

were evaluated in three different stress multiaxially conditions including bulk adhesive tensile test, thick adherends shear test and butt joints tensile test. Based on this result, whether hydrostatic sensitivity parameter which is key parameter of exponential Drucker-Prager criterion depends on stress multiaxially was examined.

Chapter 5 is the conclusion of this thesis. It summarizes the main achievements of this study and their significance, and also discusses future prospects.

References

[1] T. Hattori, S. Sakata, T. Hatsuda, G. Murakami. A stress singularity parameters approach for evaluating adhesive strength. Trans Jpn Soc Mech Eng. 1988; 31: 718-23. https://doi.org/10.1299/kikaia.54.597

[2] T. Hattori, T. Watanabe. Standardizing of strength evaluation methods using stress singularity parameters. Trans Jpn Soc Mech Eng. 2001; 67: 1486-92. https://doi.org/10.1299/kikaia.67.1486

[3] M. Goland, E. Reissner, The stresses in cemented joints, ASME J Appl Mech. 1944; 11: A17-A27. https://doi.org/10.1115/1.4009336

[4] Azari S, Eskandarian M, Papini M, Schroeder JA, Spelt JK. Fracture load predictions and measurements for highly toughened epoxy adhesive joints. Eng Fract Mech. 2009; 76: 2039-55. https://doi.org/10.1016/j.engfracmech.2009.05.011

[5] T. Ikeda, D. Lee, N. Miyazaki, Effect of Bond Thickness on the Fracture Toughness of Adhesive Joints and Its Mechanism. J Adhes Soc. 2006; 3: 97-105. https://doi.org/10.11618/adhesion.42.97

[6] Shahverdi M, Vassilopoulos A P, Keller T. Mixed-mode quasi-static failure criteria for adhesively-bonded pultruded GFRP joints. Compos Part A-Appl S. 2014; 59: 45-56. https://doi.org/10.1016/j.compositesa.2013.12.007

[7] Ducept F, Gamby D, Davies P. A mixed-mode failure criterion derived from tests on symmetric and asymmetric specimens. Compos Sci Technol. 1999; 59(4): 609–19. https://doi.org/10.1016/S0266-3538(98)00105-5

[8] Fernlund G, Spelt J K. Mixed-mode fracture characterization of adhesive joints. Comp Sci Technol. 1994; 50(4): 441-9. https://doi.org/10.1016/0266-3538(94)90052-3

[9] Ameli, A., Papini, M., Schroeder, J.A., and Spelt, J.K., Fracture R-curve characterization of toughened epoxy adhesives. Eng Frac Mech. 2010; 77: 521-34. https://doi.org/10.1016/j.engfracmech.2009.10.009

[10] Hafiz, T A, Abdel Wahab, M M, Crocombe, A D and Smith, P A, Mixed-mode fracture of adhesively bonded metallic joints under quasi-static loading Eng Fract Mech. 2010; 77: 3434-45.
https://doi.org/10.1016/j.engfracmech.2010.09.015.
[11] M.A.S. Santos, R.D.S.G. Campilho. Mixed-mode fracture analysis of composite bonded joints considering adhesives of different ductility. Int J Fract. 2017; 207: 55-71.
https://doi.org/10.1007/s10704-017-0219-x
[12] T.E.A. Ribeiro, R.D.S.G. Campilho, L.F.M. da Silva, L. Goglio. Damage analysis of composite–aluminium adhesively-bonded single-lap joints. Compos Struct. 2016; 136: 25-33.
https://doi.org/10.1016/j.compstruct.2015.09.054
[13] Elena M. Moya-Sanz, Inés Ivañez, Shirley K. Garcia-Castillo. Effect of the geometry in the strength of single-lap adhesive joints of composite laminates under uniaxial tensile load. Int J Adhes Adhes. 2017; 72: 23-29.
https://doi.org/10.1016/j.ijadhadh.2016.10.009
[14] R.D.S.G. Campilho, M.D.Banea, J.A.B.P.Neto, L.F.M.da Silva. Modelling adhesive joints with cohesive zone models effect of the cohesive law shape of the adhesive layer. Int J Adhes Adhes. 2013; 44: 48-56.
http://dx.doi.org/10.1016/j.ijadhadh.2013.02.006
[15] R.L. Fernandes, R.D.S.G. Campilho. Numerical evaluation of dissimilar cohesive models to predict the behavior of Double-Cantilever Beam specimens. Procedia Struct Integrity. 2016; 1: 42-9.
https://doi.org/10.1016/j.prostr.2016.02.007
[16] Yabin Yan, Takashi Sumigawa, Fulin Shang, Takayuki Kitamura. Cohesive Zone Criterion for Cracking along the Cu/Si Interface in Nanoscale Components. Engng Fract Mech. 2011; 78(17): 2935-46.
https://doi.org/10.1016/j.engfracmech.2011.08.010
[17] Ting Miao, Liqiong Tian, Xiaochang Leng, Zhamgmu Miao, Chengjun Xu. A Comparative Study of Cohesive Zone Models for Predicting Delamination Behaviors of Arterial Wall. Open Physics. 2020; 18: 467–477.
[18] M.F.S.F. De Moura, J.P.M. Gonçalves, J.A.G. Chousal, R.D.S.G. Campilho. Cohesive and continuum mixed-mode damage models applied to the simulation of the mechanical behaviour of bonded joints. Int J Adhes Adhes. 2008; 28(8): 419-26.
https://doi.org/10.1016/j.ijadhadh.2008.04.004
[19] Campilho RDSG, de Moura MFSF, Domingues JJMS. Using a cohesive damage model to predict the tensile behaviour of CFRP single-strap repairs. Int J Solids Struc.

2008; 45: 1497–512.
https://doi.org/10.1016/j.ijsolstr.2007.10.003
[20] M.N. Cavalli, M.D. Thouless. The Effect of Damage Nucleation on the Toughness of an Adhesive Joint. J Adhesion. 2001; 76: 75-92.
https://doi.org/10.1080/00218460108029618
[21] Campilho RDSG, Banea MD, Neto JABP, et al. Modelling adhesive joints with cohesive zone models: effect of the cohesive law shape of the adhesive layer. Int J Adhes Adhes. 2013; 44: 48–56.
https://doi.org/10.1016/j.ijadhadh.2013.02.006.
[22] Kenane, M., Benzeggagh, M.L. Mixed-mode delamination fracture toughness of unidirectional glass/epoxy composites under fatigue loading. Compos Sci Technol. 1997; 57 (5): 597–605.
https://doi.org/10.1016/S0266-3538(97)00021-3
[23] Balzani C, Wagner W, Wilckens D, Degenhardt R, Büsing S, Reimerdes HG. Adhesive joints in composite laminates-A combined numerical/experimental estimate of critical energy release rates. Int J Adhes Adhes. 2012; 32: 23–38.
https://doi.org/10.1016/j.ijadhadh.2011.09.002
[24] Mathews M, Swanson SR. Characterization of the interlaminar fracture toughness of a laminated carbon/epoxy composite. Compos Sci Technol. 2007; 67: 1489–98.
https://doi.org/10.1016/j.compscitech.2006.07.035
[25] Bui QV. A modified Benzeggagh-Kenane fracture criterion for mixed-mode delamination. J Compos Mater. 2011; 45(4): 389–413.
https://doi.org/10.1177/0021998310376105
[26] F.A.A. Nunes, R.D.S.G. Campilho, Mixed-mode fracture analysis of adhesively-bonded joints using the ATDCB test specimen. Int J Adhes Adhes. 2018; 85: 58-68.
https://doi.org/10.1016/j.ijadhadh.2018.05.019
[27] Wang CH, Rose LRF. Determination of triaxial stresses in bonded joints. Int J Adhesion Adhesives. 1997; 17: 17-25.
https://doi.org/10.1016/S0143-7496(96)00028-0
[28] Chun HW, Peter C. Plastic yielding of a film adhesive under multiaxial stresses. Int J Adhes Adhes. 2000; 20: 155-64.
https://doi.org/10.1016/S0143-7496(99)00033-0
[29] Bagheri R, Pearson R A. Role of particle cavitation in rubber-toughened epoxies:
1. Microvoided toughening. Polymer. 1996; 37: 4529-38.
https://doi.org/10.1016/0032-3861(96)00295-9
[30] Makoto Imanaka, Ryousuke Orita, Yosinobu Nakamura, Masaki Kimoto.

Comparison of failure mechanisms between rubber-modified and unmodified epoxy adhesives under mode II loading condition. J. Mater. Sci. 2008; 43: 3223-33. https://doi.org/10.1007/s10853-008-2557-6
[31] Kinloch A J, Shaw S J, Tod D A, Hunston DL. Deformation and fracture behavior of a rubber-toughened epoxy:1. Microstrucuture and fracture studied. Polymer. 1983; 24: 1341-54. https://doi.org/10.1016/0032-3861(83)90070-8
[32] Pearson R A, Yee A F. Toughening mechanisms in elastomer-modified epoxies Part 2 Microscopy studies. J. Mat. Sci. 1986; 21: 2475-88. https://doi.org/10.1007/BF01114294
[33] Dean G, Crocker L, Read B, Wright L. Prediction of deformation and failure of rubber-toughened adhesive joints. Int J Adhes Adhes. 2004; 24: 295-306. https://doi.org/10.1016/j.ijadhadh.2003.08.002
[34] Garcı´a JA, Chiminelli A, Garcı´a B, Lizaranzu M, Jiménez MA. Characterization and material model definition of toughened adhesives for finite element analysis. Int J Adhe Adhes. 2011; 31: 182-92. https://doi.org/10.1016/j.ijadhadh.2010.12.006
[35] Chiminelli A, Breto R, Jiménez MA, Velasco F, Abenojar J, Martínez MA. Experimental method for the determination of material parameters of plasticity models for toughened adhesives. Int J Adhes Adhes. 2016; 68: 182-7. https://doi.org/10.1016/j.ijadhadh.2016.03.004
[36] Quan H, Alderliesten R. On the effect of plastic model on simulation of adhesive bonded joints with FM94. Int J Adhes Adhes. 2021; 110: 102916. https://doi.org/10.1016/j.ijadhadh.2021.102916

Chapter 2 Mixed-mode fracture toughness evaluation of adhesive joints

2.1 Introduction

In practical adhesive structures, the adhesive joints are subjected to complicated stress conditions due to their complexity of the cross-sectional geometry and the multi-directional loading. Therefore, evaluation method that account for combined stress is necessary to predict the strength of the adhesive joints.

Toughened epoxy adhesive is prominently used in structural component such as airframes, turbine blades and repair for the CFRP components. Some toughened adhesives are characterized by crack propagation before failure. Therefore, it is important to be able to predict crack propagation behavior under mixed-mode conditions. It is necessary to clarify the *R*-curve behavior of highly toughened epoxy adhesives under the various mode ratios.

MMB test and Arcan test are well-known methods for evaluating mixed-mode fracture toughness. These methods cover a wide range of mixed-mode loading conditions from mode I to mode II and used to assess the mixed-mode interlaminar fracture toughness of CFRP or the fracture toughness of adhesive bonded joints. The MMB test has a unique characteristic that combines the DCB test and the 3-point bending end-notched flexure (ENF) test. In the MMB test, the crack tip approaches the loading punch as the crack propagates, so the energy release rate is affected by the external force from the punch [1]. The Arcan test is not appropriate for evaluating fracture toughness along with crack propagation because the specimen is as small as the compact tension (CT) test and the ligament length is short. For this reason, this study uses the link-type jig proposed by Fernlund-Spelt [2], in which the crack tip is less affected by the constraint of the apparatus and can accommodate longer crack length. This jig enables accurate evaluation of fracture toughness during crack propagation.

This chapter intends to evaluate the fracture toughness of adhesives during crack propagation in mixed-mode conditions by using theoretical method and FEM. The mixed-mode fracture toughness tests are performed using a link-type jig proposed by Fernlund-Spelt. The characteristic of *R*-curve behavior is evaluated up to crack length of 25 mm from initiation. The goal is to validate the *J*-integral of fracture toughness tests using FE analysis by comparing the energy release rate at crack propagation with experimental results, and to establish an analytical method for the energy release rate in link-type fracture toughness test jig.

2.2 Loading system of mixed-mode fracture toughness test

Fig. 2.1 presents the mixed-mode loading system that proposed by Fernlund-Spelt, featuring a mechanical link with hinge and arm.

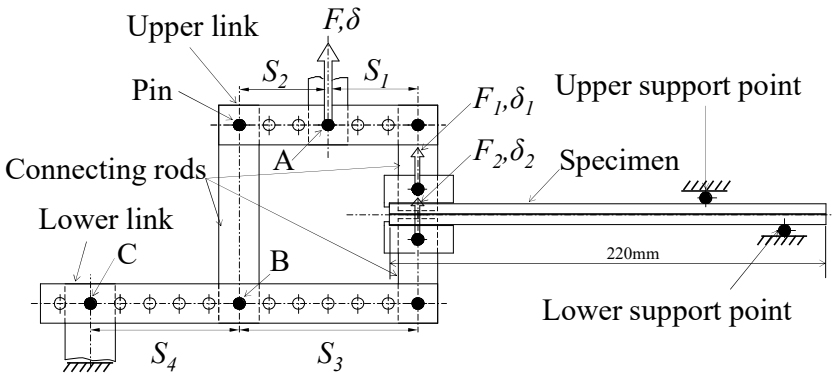

Cross section of upper and lower links	width:20mm,thickness:20mm
Cross section of connecting rods	width:20mm,thickness:6mm

Fig. 2.1 Mixed mode loading system proposed by Fernlund-Spelt [2].

This jig enables the DCB specimen to be subjected to bending deformation while opening crack, giving Mode I and Mode II deformations simultaneously, and allows the fracture toughness tests under a wide range of mixed-mode conditions. The characteristics of the apparatus are as follows.

1) Due to the relatively longer distance between the loading point and the support point compared to other jigs, it can provide sufficient ligament length.
2) By setting the pins in the adequate position the mode ratio can be changed.
3) Mode ratio can be determined by changing the hinge distance.

Therefore, it is possible to obtain *R*-curves of adhesive joints with crack propagation at various mode ratios.

2.3 Evaluation method for mixed-mode energy release rate

2.3.1 Energy release rate based on beam theory and mode partitioning

According to Spelt et al. [2] the energy release rate for the jig shown in Fig. 2.1 can be derived as follows. The DCB specimen was supported at upper-rod and lower-rod, and it was subjected to loads F_1 and F_2 by constraining the vertical displacement of the right end. The applied loads F_1 and F_2 for a given jig load F can be determined by S_i $(i = 1, 2, 3, 4)$ as follows:

$$F_1 = F\frac{S_2}{S_3}, \qquad (2.1)$$

$$F_2 = F\frac{S_1 S_4}{S_3(S_3+S_4)}, \qquad (2.2)$$

where S_i denote the lengths between each pin. Note that mixed mode ratios (G_{II}/G_T) can be defined by S_i just changing the pin arrangement in the jig. The mixed-mode ratio given as a function of F_1 and F_2 will be discussed later.

Based on the Bernoulli-Euler beam theory, neglecting the adhesive layer, the total energy release rate G in the DCB test for given loads F_1 and F_2 is given by:

$$G = \frac{P^2}{2B}\frac{dC}{da} = \frac{6(F_1 a)^2}{B^2 E h^3}\left[1 + \left(\frac{F_2}{F_1}\right)^2 - \frac{1}{8}\left(1 + \left(\frac{F_2}{F_1}\right)\right)^2\right], \qquad (2.3)$$

where B and h are the width and thickness of the adherend, respectively, a is the crack length, and E is the Young's modulus of the adherend. Since unidirectional CFRP was used as the adherend, the Young's modulus E was replaced with E_{11}, that is elastic modulus in the fiber direction. Note that Eq. 2.3 neglects the adhesive layer.
The phase angle of loading ψ was defined as:

$$\psi = \arctan\left[\frac{\sqrt{3}}{2}\frac{\left(\frac{F_1}{F_2}+1\right)}{\left(\frac{F_1}{F_2}-1\right)}\right] \qquad (2.4)$$

The energy release rates in mode I and II are given by:

$$G_I = G\left[\frac{1}{1+\tan^2(\psi)}\right] \qquad (2.5)$$

$$G_{II} = G\left[\frac{\tan^2(\psi)}{1+\tan^2(\psi)}\right] \qquad (2.6)$$

2.3.2 Energy release rate considering adhesive layer

Fernlund and Spelt [3] further considered the elastic deformation of the adhesive layer based on the theory of a beam placed on an elastic support as follows. The external forces F_1 and F_2 are separated into mode I component f_1 and mode II component f_2, respectively, as

$$f_1 = \frac{F_1 - F_2}{2}, \qquad (2.7)$$

$$f_2 = -\frac{F_1 + F_2}{2}. \qquad (2.8)$$

Then the energy release rate, considering adhesive thickness t, is given by the equation:

$$G = \frac{P^2}{2B}\frac{dC}{da} = \frac{12a^2}{B^2E(h-t)^3}\left[f_1^2\Phi_I^2 + \frac{3}{4}f_2^2\Phi_{II}^2\right], \qquad (2.9)$$

where a is crack length, and E and h are elastic modulus of the adherend and thickness, respectively. Φ_I and Φ_{II} are given by the equations:

$$\Phi_I = 1 + 0.667\frac{h}{a}\left[\left(1 - \frac{t}{h}\right)^3\left[1 + \frac{t}{h}\left(\frac{2E}{E_a} - 1\right)\right]\right]^{0.25}, \qquad (2.10)$$

$$\Phi_{II} = 1 + 0.206\frac{h}{a}\sqrt{\left[1 - \frac{t}{h}\right]\left[1 + \frac{2tE\alpha}{G_a h}\right]}, \qquad (2.11)$$

where $\alpha = 2.946$ is a calibration constant determined by a FE analysis [4]. E_a and G_a are the elastic and shear modulus of adhesive, respectively. The phase angle is given by the following equation:

$$\psi = \arctan\left[\frac{\sqrt{3}}{2}\frac{f_2\Phi_{II}}{f_I\Phi_I}\right]. \qquad (2.12)$$

In addition, the total energy release rate G is separated into the individual energy release rates G_I and G_{II}, which are calculated by Eqs. 2.5 and 2.6 using the phase angle ψ.

2.4 Validation of mode ratio using FE analysis

2.4.1 FE model

In order to evaluate the *R*-curve accurately, whether the mode ratio with respect to crack propagation would be remained constant was examined using FE analysis. Specifically, the theoretical values of G_I and G_{II} derived with Eq. 2.9 were compared with those derived from the FE analysis.

A two dimensional (2D) linear elastic FE analysis was conducted with the FE code

MSC-Marc. The experimental loading devices were modeled by a combination of beam and links. Prior to conducting the FE analysis using beam and link elements, it was confirmed that the values F_1 and F_2 calculated from the FE analysis agreed with the values obtained from the given F according to Eqs. 2.1 and 2.2.

The DCB specimen was modeled with plane strain four node quadrilateral elements. The adhesive layer was meshed with twelve elements across the thickness. The crack was introduced by double nodes along edges of elements on the middle of adhesive thickness. The size of the element at the crack tip was 0.015 mm. The overall mesh and boundary conditions are illustrated in Fig. 2.2. Load F was applied at point B. The movement of the specimen was constrained in the vertical direction at its right end. The mechanical properties used in this simulation are presented in Table 2.1. Subscripts 1, 2 and 3 used in the table correspond to fiber direction, width direction and thickness direction of adherend, respectively.

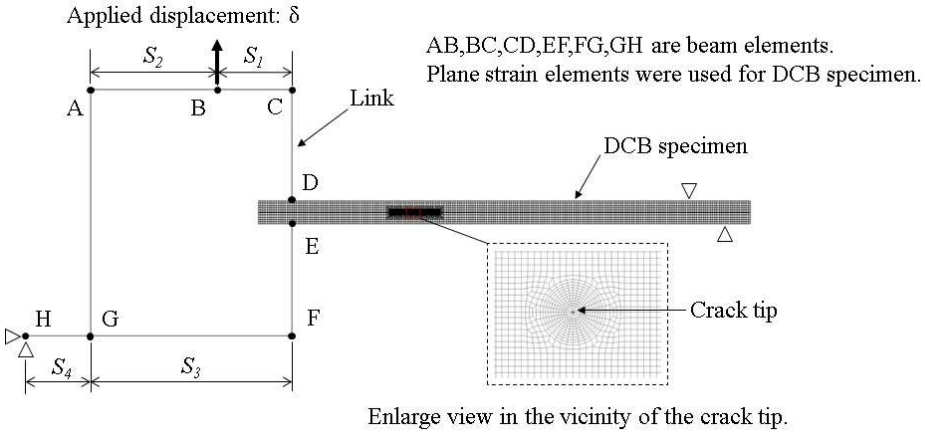

Fig. 2.2 Boundary conditions and mesh pattern for FE analysis.

Table 2.1 Mechanical properties of adhesive and adherend.

Adherend (unidirectional CFRP)

Young's modulus (GPa)			Poisson's ratio			Shear modulus (GPa)		
E_{11}	E_{22}	E_{33}	v_{12}	v_{23}	v_{31}	G_{12}	G_{23}	G_{31}
130	9.9	9.9	0.31	0.21	0.02	4.0	7.5	4.0

Adhesive (Filmy type epoxy adhesive)

Young's modulus (GPa)	Poisson's ratio
E	v
1.81	0.34

The energy release rate was calculated using the virtual crack closure technique (VCCT), for the load F of 100 N. The analysis was performed under the mode ratio G_{II}/G_T of 0.8, 0.68, 0.55 and 0.21 with the crack length a of 0 mm, 10 mm, 20 mm, 40 mm, 60 mm. The geometric nonlinearity is considered in this analysis. The effect of any residual stress was not considered in the analysis.

2.4.2 FE results

The mode ratio behaviors as a function of the crack length under the given specific mode ratios were compared between the theoretical values and FE results. The mode ratio G_{II}/G_T as a function of crack length a, defined by the beam theory and FE analysis is presented in Fig. 2.3. As shown in this figure, it was confirmed that the mode ratio G_{II}/G_T keeps an almost constant value throughout the crack length. This figure also shows that the mode ratio obtained by the FE analysis agrees well with that calculated by the beam theory irrespective of crack length.

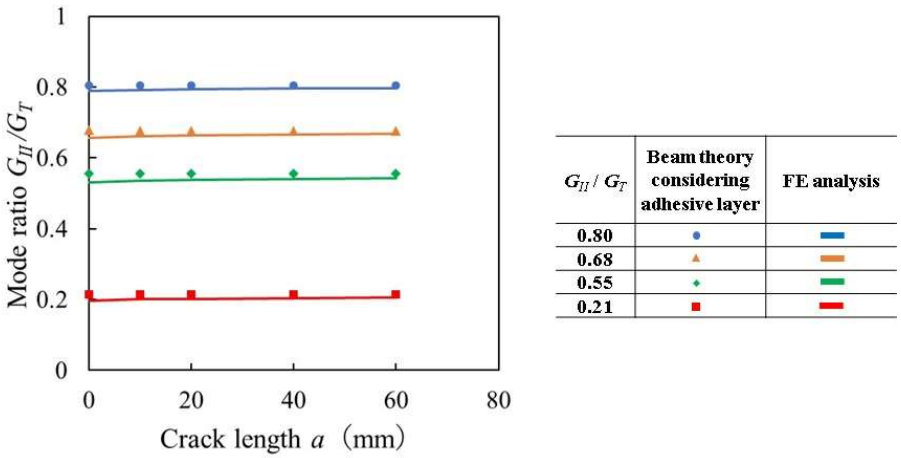

Fig. 2.3 Relationship between mode ratio and crack length.

2.5 Fracture toughness test of CFRP adhesive joints under mixed-mode condition

2.5.1 Materials

The material of adherend is as follows. Unidirectional CFRP prepreg sheets with a nominal thickness of 0.2 mm were used as an adherend of the DCB specimen. The fiber of the CFRP was TR50S and the matrix resin was #350, Mitsubishi chemical. The unidirectional CFRP prepregs were stacked as $[0°]_{40}$ and placed in a vacuum bag then cured in autoclave under the pressure of 0.2 MPa and a temperature of 130°C. The mechanical properties of the CFRP are listed in Table 2.1.

The adhesive used for the DCB specimen was film epoxy adhesive (AF163-2U,

nominal thickness of 0.14 mm, 3M). The material properties of adhesive were obtained by tensile test. The preparation of specimen is as follows. The 24 laminated adhesive film was put in a bag and vacuumed for a few minutes to avoid air inclusions. Then, it was clamped between release-treated steel plates via 3 mm thickness gauges and cured at 120℃ for 1 h. After cooling to the room temperature, the bulk adhesive plate was trimmed into a dumbbell shape specimen. The shape and dimensions of the specimen are shown in Fig. 2.3.

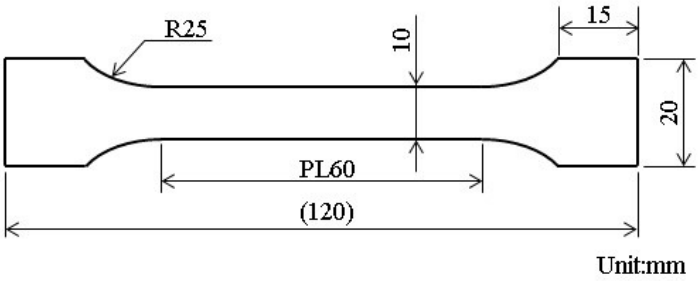

Fig. 2.3 Shape and sizes of dumbbell specimen for tensile test (Thickness = 3.0 mm).

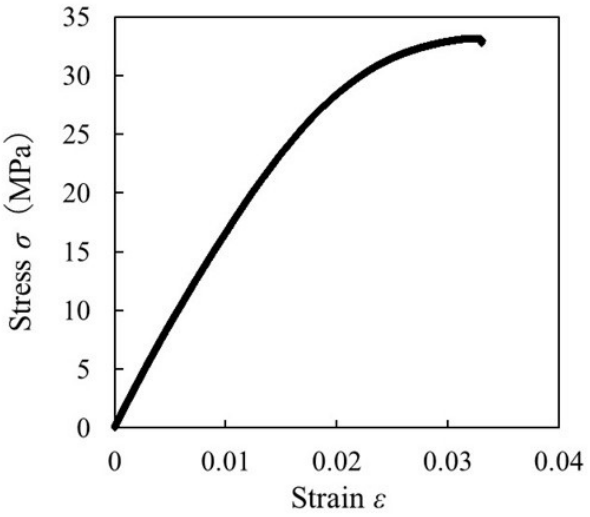

Fig. 2.4 Stress-strain curve of the bulk adhesive.

The test method is as follows. A quasi-static tensile test was conducted using a tensile test machine (AG-Xplus, Shimadzu) at room temperature and the test speed of 0.5 mm/min, while the strain was measured with an extensometer (SIE-560SA, Shimadzu).

The stress-strain curve of the bulk adhesive is shown in Fig. 2.4. Young's modulus and Poisson's ratio were obtained from the slope of the elastic region of stress-strain curve, as presented in Table 2.1.

2.5.2 Preparation of the DCB specimen

The DCB specimen used for the mixed-mode fracture test is shown in Fig. 2.5. The preparation of the specimen was as follows. Prior to bonding, the bonding surface was polished with emery paper #180, and cleaned with acetone to remove dust, oil, and release agents. Two layers of the film adhesive were placed between the adherends. A 0.01 mm thick metal film coated with a release agent was inserted in the middle of adhesive layer to induce initial crack. Polytetrafluoroethylene (PTFE) films were placed between the adherend to control the adhesive thickness, resulting a nominal value of 0.2 mm. The specimen was clamped by clips and cured in the thermostatic chamber at 120℃ for 1 h. To observe the crack propagation behavior clearly, the side of the joints was polished with emery paper #1500 along the adhesive layer after removing the excess adhesive.

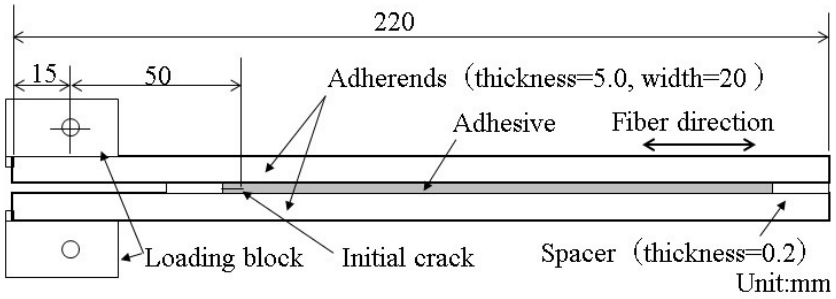

Fig. 2.5 Shape and sizes of adhesively bonded DCB specimen.

2.5.3 Test procedure

Fracture toughness tests were conducted using the Fernlund-Spelt loading jig described as in Fig. 2.6. As schematically illustrated in Fig. 2.1, the DCB was supported at upper and lower points in the end, subsequently the loads F_1 and F_2 were applied via pins attached to the adherends. The load F and the crosshead displacement δ at the point A were measured by a loadcell and an encoder mounted on the test machine, respectively, and they were recorded during the test with a frequency of 5 Hz. The crack tip image was recorded using an optical microscope camera mounted on an XYZ stage. The crack growth length was measured by the displacement of the stage using a linear gauge (LG-1100 N, Mitsutoyo). The test was conducted with a test machine (AG-100NE, Shimadzu) at a crosshead speed of 0.5 mm/min. Three mixed-mode conditions $G_{II}/G_T = 0.21, 0.55, 0.80$ and DCB test corresponding to $G_{II}/G_T = 0$ were conducted.

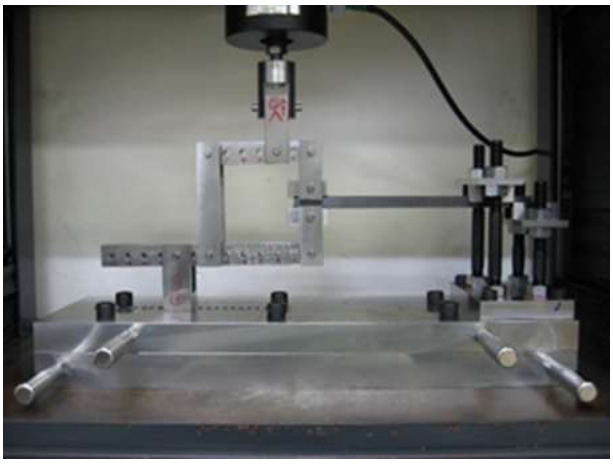

Fig. 2.6 Experimental setup using the Fernlund-Spelt loading jig for mode ratio $G_{II}/G_T = 0.55$.

2.6 Experimental results and discussion

2.6.1 Fracture toughness tests

The load-displacement curves and crack growth behaviors for various mode ratios are shown in Fig. 2.7. Additionally, microscopic images of the crack tip for crack lengths of 0.2 – 5.0 mm are also indicated. The direction of crack propagation is from left to right. The load-displacement curves are almost linear up to the maximum load.

In the condition close to Mode I side, crack tip could be found relatively clear. On the other hand, the condition close to Mode II side, it was difficult to confirm where the crack tip due to microcracks occur in front of the crack tip. The microcracks occurred in front of the crack in accordance to the increase in Mode II component. In this study, microcracks generated discontinuously at the crack tip were not regarded as cracks. The crack length was determined with the tip of the microcracks connected to the main crack at the crack tip. The approximate crack growth rates were measured and ranged from approximately 0.07 mm/sec to 0.18 mm/sec. This figure indicates following facts.

(1) In the cases of $G_{II}/G_T = 0$ and 0.21, the crack propagation initiates at the peak load, and then the crack grows with decreasing load. The crack propagated almost straightly along the adhesive-layer line.
(2) In the cases of $G_{II}/G_T = 0.55$ and 0.80, the crack propagation starts before the load reaches the maximum load. The crack propagated by the microcracks connecting to the front of the main crack. The microcracks were inclined at approximately $45°$ with respect to the adhesive-layer line.

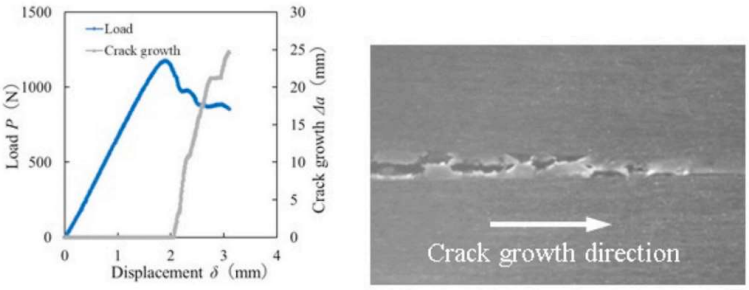

(a) $G_{II}/G_T = 0.00$ (Mode I is dominant.)

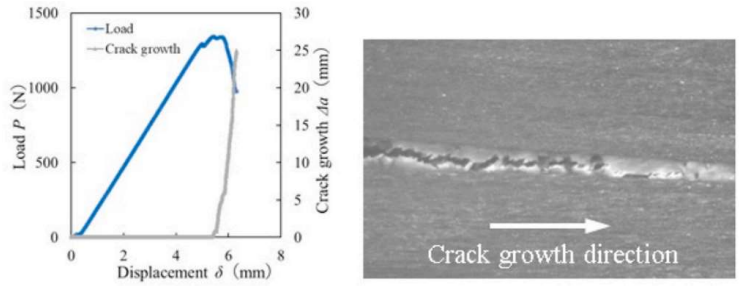

(b) $G_{II}/G_T = 0.21$ (Mode I is dominant.)

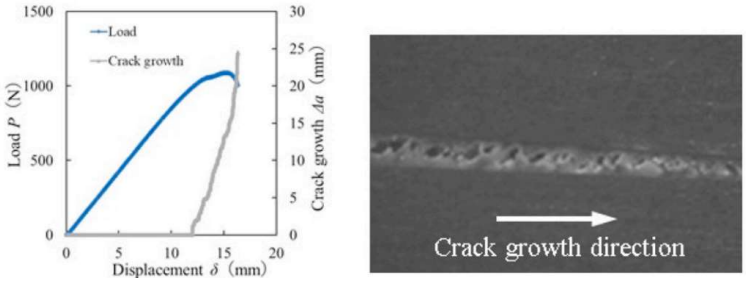

(c) $G_{II}/G_T = 0.55$ (The effect of mode II is remarkable.)

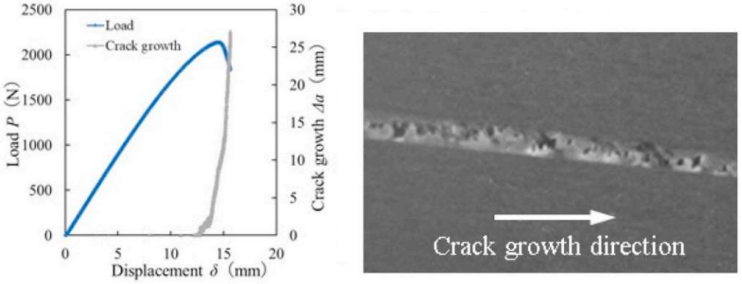

(d) $G_{II}/G_T = 0.80$ (The effect of mode II is remarkable.)

Fig. 2.7 Load-displacement and crack extension-displacement curves and microscopic images of adhesive layer for typical mode ratios.

(3) In the case of $G_{II}/G_T = 0.80$, coalescence of micro-cracks was observed at the front of the crack tip. A similar behavior in the vicinity of the crack tip under mode II loading condition was observed in the previous study by Blackman et al [5].

In the mixed-mode conditions ($G_{II}/G_T \geq 0.55$) where the shear mode was dominant, the crack propagation behavior was almost the same as in the pure shear mode condition, where microcracks appeared at the crack tip before crack propagation and they connected with each other. This is one of new findings in this work.

2.6.2 Damage zone length

The damage zone length was measured using the images recorded during mixed-mode fracture tests. The damage zone was defined as the area where stress whitening and microcracks are confirmed in front of the crack tip. The length of the damage zone is the distance from the crack tip to the end of the damage zone. The relationship between the length of damage zone and the crack growth is shown in Fig. 2.8. This figure indicates following facts.

(1) Under the mode I loading, the damage length L is almost constant regardless of the crack growth Δa.
(2) The damage length increases as mode II component increases.
(3) The damage growth rate $\Delta L/\Delta a$ increases as mode II component increases.

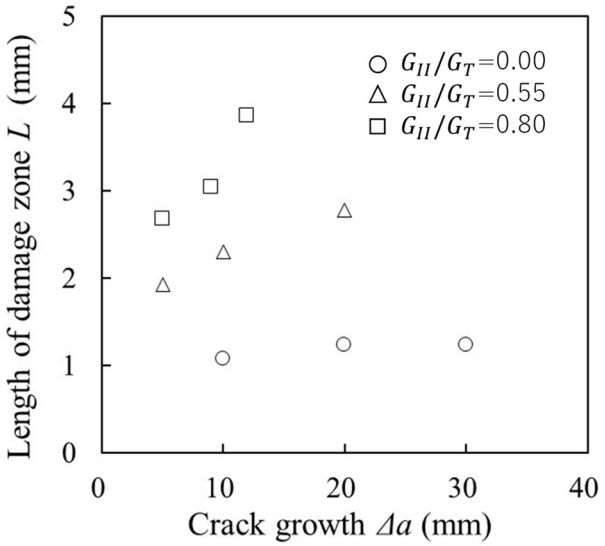

Fig. 2.8 Relationship between length of damage zone and crack growth.

2.6.3 Fracture surface-roughness

The fracture surface of the adhesive exhibits various morphologies and characteristics depending on the mode ratio. The observation of the fracture surface of the DCB specimen was conducted in order to investigate what kind of relationships or characteristics exist between mode ratios and fracture surfaces. The microscopic surface morphology was observed using the digital microscope (VR-3050, Keyence). The fracture surface roughness was determined by means of the area roughness parameter S_a (arithmetical mean height) which is the extension of R_a (arithmetical mean height of a line) to a surface. It expresses the difference in height of each point compared to the arithmetical mean height of surface.

Typical 3D digital microscopic images of the fracture surfaces for various mode ratios are shown in Fig. 2.9. The crack growth direction is from left to right. Size of the observation area is 8 mm × 8 mm, and its position is just ahead of the initial crack tip. The contour level indicates the height of the fracture surface. This figure indicates following facts.

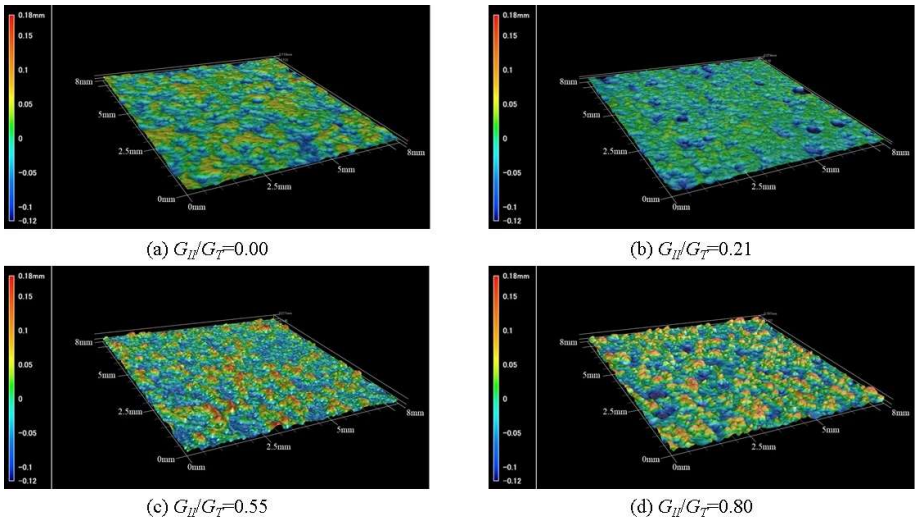

(a) G_{II}/G_T=0.00 (b) G_{II}/G_T=0.21

(c) G_{II}/G_T=0.55 (d) G_{II}/G_T=0.80

Fig. 2.9 Microscopic view of fracture surfaces for typical mode ratios.

(1) In the cases of G_{II}/G_T =0 and 0.21, surface roughness is relatively flat. This implies that the crack propagates almost straight along the adhesive-layer as shown in Figs 2.7 (a) and (b).

(2) In the cases of G_{II}/G_T =0.55 and 0.80, the small crests are found on the surface. The surface roughness is significantly higher than those in the cases of G_{II}/G_T =0 and 0.21. This also implies that the crack progresses while the microcracks are connected to the

front of the main crack, as shown in Figs 2.7 (c) and (d).
(3) The surface roughness was found to be the highest in the case of $G_T = 0.80$. This implies that the microcracks coalesce with each other during crack propagation in the mode II predominant condition.

The surface roughness parameters for various mode ratios are summarized in Fig. 2.10. This figure shows that S_a increases with the increase in the mode II component. This is because the crack propagation path develops a more complicated shape as the mode II component increases.

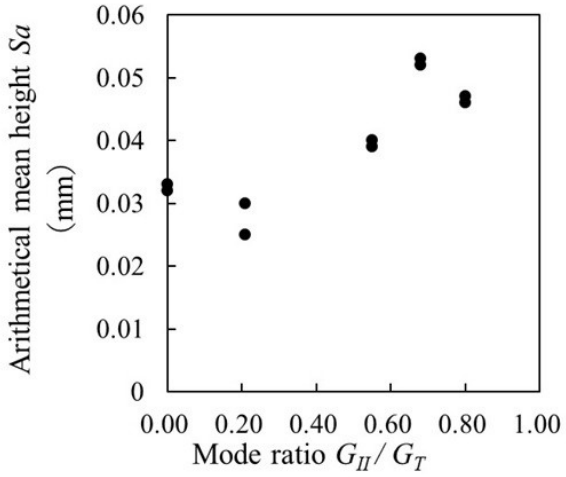

Fig. 2.10 Relationship between surface roughness and mode ratio.

2.6.4 SEM observation of fracture surfaces

The fracture surfaces were observed with a SEM (JSM-6510A, JEOL). Figure 2.11 shows the SEM observation images of the fracture surfaces for the mode ratios of $G_{II}/G_T = 0$, 0.21, 0.55, and 0.80, respectively, which correspond to those in Fig. 2.9.

In the case of $G_{II}/G_T = 0$, fracture surface was found to be relatively flat and many voids of approximately 1 μm in diameter were observed. These voids would be induced by cavitation of the rubber particles contained in the adhesive due to the high tri-axial tensile stress under mode-I loading condition [6-8].

In the case of $G_{II}/G_T = 0.21$, voids were also observed because mode I still be dominated. However, deformation of hackle patterns different from $G_{II}/G_T = 0$ was observed on the surface. This would be due to the deformation of mode II component.

In the case of $G_{II}/G_T = 0.55$ and 0.8, the hackle pattern deformation became more

significant with an increasing mode II component. Note that even under a high mode II condition, the voids were still observed.

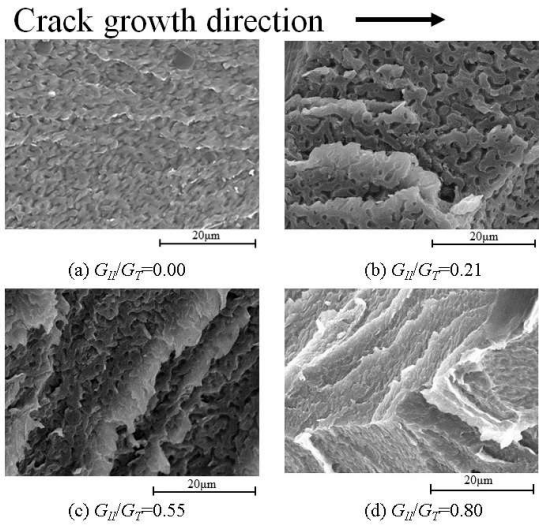

Fig. 2.11 SEM observation of fracture surfaces for typical mode ratios.

2.7 Fracture toughness based on *J*-integral

2.7.1 FE models

Fracture toughness value was evaluated with FE model using *J*-integral method to compare with theoretical value. The *J*-integral is considered more appropriate for evaluating the energy release rate of toughened adhesive than VCCT, because *J*-integral is less sensitive to the mesh shape of the crack tip. Especially in the Mode II side conditions, the mesh at the crack tip could be distorted and affect the value of the energy release rate.

The FE models were same as shown in Fig. 2.2. The *J*-integral was adopted in the crack tip instead of VCCT. The *J*-integral path was performed along an arbitrary mesh group encircling the crack tip of the adhesive layer.

2.7.2 Comparing experiment and FE results

Figure 2.12 shows the relation between the total energy release rate, G_T, and crack growth, Δa, for various mode ratios. G_T was calculated by the three methods, simple beam theory, beam theory considering adhesive layer, and *J*-integral of FE analysis, respectively.

The energy release rates calculated by the beam theory considering the adhesive layer are almost the same as those in the FE results. The results calculated by the simple

beam theory are apparently lower than those obtained with the FE results.

The difference in G_T between the simple beam theory and the FE model was found to be more significant in the region of high mode II component. Hafiz et al. [9] also reported for an adhesively bonded steel joint with a brittle adhesive that the energy release rate calculated by FEM agrees well with the energy release rate calculated by Eq. 2.9 considering the adhesive layer. From these results, it would be concluded that the consideration of the adhesive layer is of vital importance for accurate G_T calculation.

Figure 2.12 also indicates that G_T was almost constant independently of the crack length in the cases of G_{II}/G_T =0 and 0.21, whereas in the cases of $G_{II}/G_T = 0.55$, 0.68, and 0.80, it increases with the crack growth up to an approximately 10 mm. Azari et al. [10] reported that the slope of the *R*-curve increased with the increase in the ratio of mode II. This characteristic of *R*-curve agrees with that of the relationship between length of damage zone and crack growth as shown in Fig. 2.10.

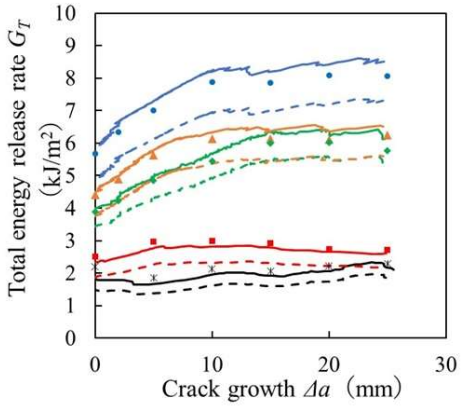

Experimental value of the total energy release rate were calculated by,
(a) Simple beam theory
(b) Beam theory considering adhesive layer
(c) FE analysis

G_{II}/G_T	(a)	(b)	(c)
0.80	- -	——	•
0.68	- -	——	▲
0.55	- -	——	◆
0.21	- -	——	■
0.00	- -	——	*

Fig. 2.12 Relationship between total energy release rate and crack growth with various mode ratios.

2.7.3 *R*-curve behavior

Figure 2.13 depicts the relationship between the total energy release rate G_T and the mode ratio G_{II}/G_T, along with the experimental and the corresponding FE analysis results.

This figure is used to investigate the relationship between the *R*-curve and mode ratio. Here, G_{TS} denotes the steady state energy release rate over the plateau region of the *R*-curve which was obtained by averaging G_T from 10mm to 25mm in Fig. 2.12. G_{TC} denotes the critical energy release rate at the crack initiation which means the G_T of $\Delta a = 0$ in Fig. 2.12. It was found that both G_{TC} and G_{TS} increased as a function of

G_{II}/G_T and the difference between G_{TC} and G_{TS} increased with increase of the mode II component. The other comparable studies have also indicated similar trends [10-12].

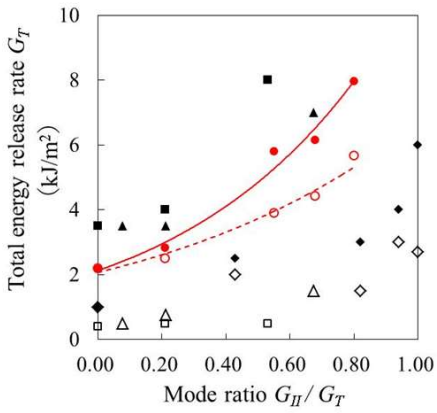

Experimental value of the total energy release rate were calculated by FE analysis.
(a) Steady state energy release rate :G_{TS}
(b) Crack initiation energy release rate : G_{TC}

	(a)	(b)
Experimental plot	●	○
Curve fit	—	----

Data from the reference paper lists.

Reference number	(a)	(b)	Adhesive and adherend
10	▲	△	Paste type epoxy adhesive/Aluminum alloy
11	■	□	Paste type epoxy adhesive/Aluminum alloy
12	◆	◇	Film adhesive(FM300-2M:Cytec Engineered Materials)/CFRP

Fig. 2.13 Relationship between total energy release rate and mode ratio.

2.7.4 Discussion

The reasons why the difference between G_{TC} and G_{TS} increased with increase of the mode II component are discussed. Generally, at the crack tip in adhesive joints under mode I loading, the stress multiaxiality is high and the plastic region is small. However, as the mode II component increases, the stress multiaxiality decreases and the plastic region expands. Therefore, it is well known that fracture toughness increases with the increase in the mode II component [5, 9, 11-12].

Furthermore, it has been also known that an increase in mode II component creates microcracks inclined toward the interface in the vicinity at the crack tip [5, 12]. Thus, the increase of the mode II component forms the complicated damage area at the crack tip where plastic region and microcracks were exist.

The reason why the difference between G_{TC} and G_{TS} increases with the increasing mode II component have explained from the viewpoint of the damage zone of mode II component [3, 11]. However, the expansion of the plastic region and damage zone contributes to the increase in both G_{TC} and G_{TS}. Therefore, only two reasons are insufficient to explain why the increase in the mode II component increases the slope of *R*-curve.

The results of this study imply that the difference between both G_{TC} and G_{TS} relates to the crack propagation appeared in Fig. 2.7. This complicated path caused rough fracture surface especially mode II dominant condition described as in Fig. 2.9. The

complicated crack path would increase the crack growth resistance. These results could explain the characteristic of the R-curve where the difference between G_{TC} and G_{TS} increases with the increase in mode II component.

2.8 Conclusions

Fracture toughness tests for adhesively bonded CFRP joints under mixed I and II mode conditions were conducted by means of the Fernlund–Spelt DCB test, where a highly toughened epoxy adhesive was used. The main findings of this study are as follows:

1. The total energy release rate G_T increased with the increase in the mode II component. In the mode ratios $G_{II}/G_T = 0$ and 0.21, G_T was almost constant irrespective of crack length, whereas in the cases of $G_{II}/G_T = 0.55$, 0.68 and 0.80, G_T increased up to approximately 10 mm crack length, then it saturated for further crack growth.
2. The difference between G_{TC} ($= G_T$ at the onset of crack growth) and G_{TS} ($= G_T$ at the steady state) increases with the increase in mode II component. This reason may occur because the crack propagation path has a more complicated shape with the increase in mode II component, and the complicated crack propagation path increases the crack growth resistance. Reflecting such crack growth behavior, the surface roughness S_a increased with the increase in mode II component. This is because the crack propagation path develops a more complicated shape as the mode II component increases.
3. From SEM observation of the fracture surfaces, under the pure mode I condition ($G_{II}/G_T = 0$), many voids induced by a high triaxial tensile stress were observed on the relatively flat fracture surface. As the mode II component increased, the pleated deformation became more dominant, wherein many voids were still observed until the mode ratio G_{II}/G_T reached 0.55. On the fracture surface for $G_{II}/G_T = 0.80$ (where the mode II component was the highest), a sharply ridged deformation was observed, wherein the growth of voids were suppressed under the low triaxial tensile-stress condition.

References

[1] Mannami Y, Nakayama M, Kitamura R, Ogihara S. Evaluation of Mixed Mode Interlaminar Fracture Properties of Stitched CFRP Laminates. J Soc Comp Mat. 2017; 43: 193-200.

https://doi.org/10.6089/jscm.43.193
[2] Fernlund G, Spelt J K. Mixed-mode fracture characterization of adhesive joints. Comp Sci Technol 1994;50(4):441-9.
https://doi.org/10.1016/0266-3538(94)90052-3.
[3] Fernlund G, Spelt J K. Mixed mode energy release rates for adhesively bonded beam specimens. J Compos Technol. 1994; 16(3) :234–43.
https://doi.org/10.1520/CTR10412J
[4] Azari S, Papini M, Schroeder J A, Spelt J K. The effect of adhesive thickness on fatigue and fracture of toughened epoxy joints-Part 1:Experiments Eng Fract Mech 2011;78:153-162. https://doi.org/10.1016/j.engfracmech.2010.06.025
[5] Blackman B R K, Kinloch A J and Paraschi M. The determination of the mode II adhesive fracture resistance, GIIC, of structural adhesive joints: An effective crack length approach. Eng Frac Mech, 2005;72:877-897.
https://doi.org/10.1016/j.engfracmech.2004.08.007
[6] Kinloch A J, Shaw S J, Tod D A, Hunston DL. Deformation and fracture behavior of a rubber-toughened epoxy:1. Microstrucuture and fracture studied. Polymer 1983;24:1341-1354. https://doi.org/10.1016/0032-3861(83)90070-8.
[7] Pearson R A, Yee A F. Toughening mechanisms in elastomer-modified epoxies Part 2 Microscopy studies. J. Mat. Sci. 1986;21:2475-2488.
https://doi.org/10.1007/BF01114294.
[8] Bagheri R, Pearson R A. Role of particle cavitation in rubber-toughened epoxies: 1. Microvoided toughening. Polymer 1996;37:4529-4538. https://doi.org/10.1016/0032-3861(96)00295-9.
[9] Hafiz, T A, Abdel Wahab, M M, Crocombe, A D and Smith, P A, Mixed-mode fracture of adhesively bonded metallic joints under quasi-static loading Eng Fract Mech 2010;77:3434-3445. https://doi.org/10.1016/j.engfracmech.2010.09.015
[10] Azari S, Eskandarian M, Papini M, Schroeder JA, Spelt JK. Fracture load predictions and measurements for highly toughened epoxy adhesive joints. Eng Fract Mech 2009;76:2039-55. https://doi.org/10.1016/j.engfracmech.2009.05.011.
[11] Ameli, A., Papini, M., Schroeder, J.A., and Spelt, J.K. Fracture R-curve characterization of toughened epoxy adhesive. Eng Frac Mech 2010;77:521-534. https://doi.org/10.1016/j.engfracmech.2009.10.009.
[12] Mohan J, Ivanković A, Murphy N. Mixed-mode fracture toughness of co-cured and secondary bonded composite joints. Eng Fract Mech. 2015;134:148-67.
https://doi.org/10.1016/j.engfracmech.2014.12.005.

Chapter 3 Crack propagation of adhesive joints using cohesive zone models under the mixed-mode conditions

3.1 Introduction

In the case of fracture mechanics problems such as cohesive failure of adhesive bonded joints, delamination of CFRP laminates, interfacial fracture of dissimilar materials and fatigue failure, the use of cohesive zone model (CZM) has been more increasing in recent years. These models are able to deal with simulation of onset of crack and propagation. In general, CZMs are implemented in FE models between solid elements or shell elements. CZMs may have specific thickness or zero thickness. Because it is not continuum elements but interfacial elements and does not have Young's modulus and Poisson's ratio, so zero thickness is not a problem. Once the behavior of traction-separation law between the element and another one is clear, CZMs can be applied.

The use of ductile adhesive has increased for vehicles because the high fracture toughness contributes the safety. Therefore, it is important to set appropriate traction-separation curve and CZM parameters for ductile adhesives. And the verification whether the CZMs could work well under the mixed-mode conditions is needed.

In this chapter the crack propagation of adhesive joints with toughened epoxy adhesive under the mixed-mode condition was evaluated. The interest of this study is to clarify whether the crack propagation for every mode ratio could predict using trapezoidal traction-separation in this adhesive. And the appropriate of the CZM's energy-based power-law failure criterion was evaluated compared to conventional liner criteria.

3.2 Traction-separation law

CZM was originally introduced to treat small scale yielding conditions at the crack tip in linear elastic fracture mechanics [1, 2]. The energy which has been consumed in the region where traction force acts between the continuum elements can deal with as failure criterion, and crack propagation can be simulated. The discretization model which was embedded into FE model of the relationship between traction and cohesive energy is CZM. This special interface element is applicable to delamination of CFRP and crack propagation of adhesive joints.

The behavior of the CZM is defined by the traction t_i and separation δ_i acting between the continuum elements, and the relationship between them is expressed in Eq. 3.1.

$$t_i = f(\delta_i) \qquad (i = I, II, III) \qquad (3.1)$$

The relationship between traction and separation is called traction-separation law. A

typical triangular shape (bilinear) traction-separation law relationship under the mode I condition is shown in Fig. 3.1.

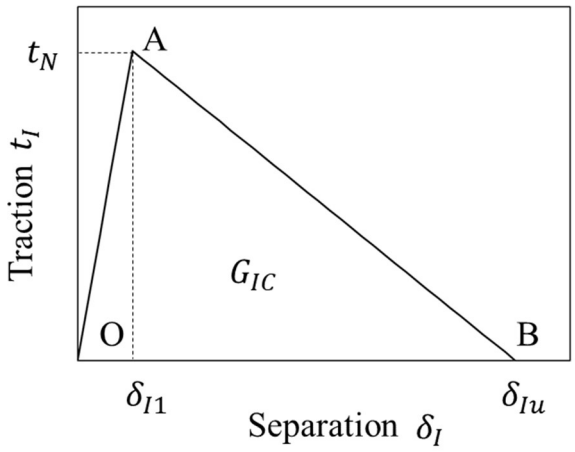

Fig. 3.1 Bilinear traction-separation law relationship under mode I condition.

The area under the traction-separation curve OAB corresponds to the energy at which CZM completely disappear. The fracture energy value of crack propagation per area G_i expressed in Eq. 3.2 is equal to the area under the traction-separation curve.

$$G_i = \int_0^{\delta_{iu}} f(\delta_i) d\delta_i \qquad (3.2)$$

The traction-separation curve between OA described as Fig. 3.1 is linear relation, and CZM functions as a linear spring. Assuming that the CZM is inserted between the 8-nodes solid element, the relationship between the traction and separation can be expressed as in Eq. 3.3.

$$t_i = \begin{Bmatrix} t_I \\ t_{II} \\ t_{III} \end{Bmatrix} = \begin{bmatrix} K_I & 0 & 0 \\ 0 & K_{II} & 0 \\ 0 & 0 & K_{III} \end{bmatrix} \begin{Bmatrix} \delta_I \\ \delta_{II} \\ \delta_{III} \end{Bmatrix} = K_i \delta_i \qquad (3.3)$$

where K_i is the elasticity matrix in the mode I, II, and III.

When CZM satisfies damage onset criterion Eq. 3.4, it corresponds to point A in Fig. 3.1. Where t_N, t_S and t_T are the maximum traction in mode I, II and III, and this equation can define the damage onset condition in three-dimensional.

$$\left(\frac{\langle t_I \rangle}{t_N}\right)^2 + \left(\frac{t_{II}}{t_S}\right)^2 + \left(\frac{t_{III}}{t_T}\right)^2 = 1 \qquad (3.4)$$

The segment AB in Fig. 3.1 represents a linear degrease in traction. If CZM meets the damage onset condition Eq. 3.4, the traction can be expressed by Eq. 3.5 using the damage variable d_i.

$$t_i = (1 - d_i) K_i \delta_i \qquad (3.5)$$

When the damage variable reaches $d_i = 1$, the CZM is considered to have completely failed, and the traction is $t_i = 0$, corresponding to point B in Fig. 3.1. The damage variable d_i can be given as:

$$d_i = \frac{\delta_{u,i}(\delta_i - \delta_{1,i})}{\delta_i(\delta_{u,i} - \delta_{1,i})} \qquad (3.6)$$

Note that δ_i is not the current separation but the maximum separation. Because the damage to CZM is not recovered by unloading.

Traction-separation law can also be given in other forms. For example, the trapezoidal shape shown in Fig. 3.2, the damage variable d_i can be given as follows.

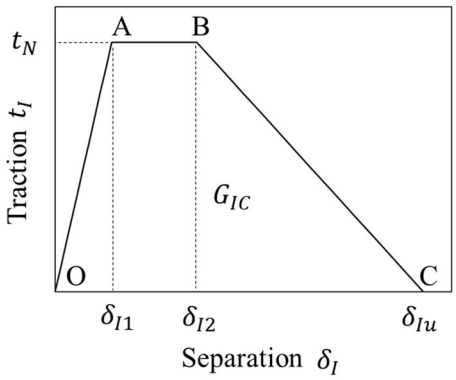

Fig. 3.2 Trapezoidal shape traction-separation relationship under the Mode I condition.

The plateau region (segment AB in Fig. 3.2) is as follows.

$$d_i = 1 - \frac{\delta_{1,i}}{\delta_i} \qquad (3.7)$$

The segment BC where traction degrease is as follows.

$$d_i = 1 - \frac{\delta_{1,i}(\delta_{u,i} - \delta_i)}{\delta_i(\delta_{u,i} - \delta_{2,i})} \qquad (3.8)$$

The energy-based failure criterion for CZM can take into account mixed-mode conditions as shown in Eq. 3.9. Here, the most representative linear criterion is shown, other mixed-mode failure criteria have also been proposed, such as the power-law and the BK law [3].

$$\left(\frac{G_I}{G_{IC}}\right) + \left(\frac{G_{II}}{G_{IIC}}\right) + \left(\frac{G_{III}}{G_{IIIC}}\right) = 1 \qquad (3.9)$$

Although this chapter presents a three-dimensional traction-separation law, the CZM of a two-dimensional four-node shell element can also be applied when the adhesive joint is employed as a plane stress or plane strain.

3.3 Critical energy release rate for CZM

3.3.1 Mode II fracture toughness

The fracture toughness values under mode I and II loading conditions are required for CZM estimation under mixed-mode conditions. In the case of CZM, how to define fracture toughness values is very important things. This study aims to deal with ductile adhesive. Since ductile adhesives have been subject to plastic deformation and microcracks during crack propagation, fracture toughness values used in CZM should be defined based on the *R*-curve characteristic. In Mode II condition, the obtaining of the relationship between energy release rate and crack length is very difficult, because the crack tip is not clear. The appropriate method for evaluating the *R*-curve under the Mode II condition has been proposed by compliance-based beam method (CBBM) [4, 5]. Therefore, ENF test for the Mode II fracture toughness value was evaluated using CBBM method.

3.3.2 ENF tests

Fig. 3.3 depicts the geometry and dimensions of the ENF specimens. Unidirectional

CFRP prepreg sheets with a nominal thickness of 0.20 mm were used as an adherend. The CFRP fiber was TR50S, and the matrix resin was #350 (Mitsubishi Chemical). The unidirectional CFRP prepregs were stacked at $[0°]_{40}$ and cured in an autoclave. A rubber-modified epoxy adhesive film (AF163-2U, 3M) was used.

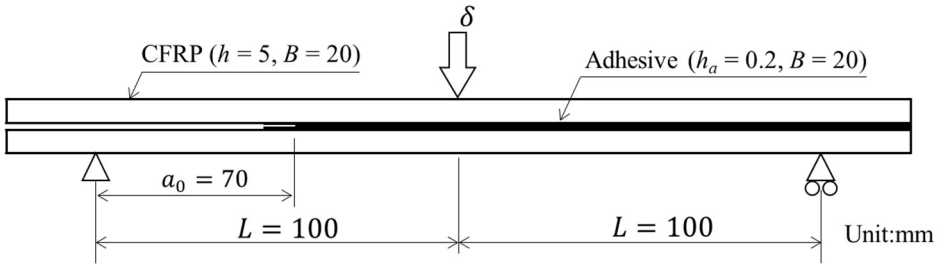

Fig. 3.3 Schematic representation of ENF test.

The ENF test was conducted under a three-point bending loading. Loading displacement was applied at the rate of 0.5 mm/min using a universal testing machine (AG-100NE, Shimadzu) to induce stable crack propagation. The experimental load–displacement $(P-\delta)$ curves for the ENF test are presented in Fig. 3.4.

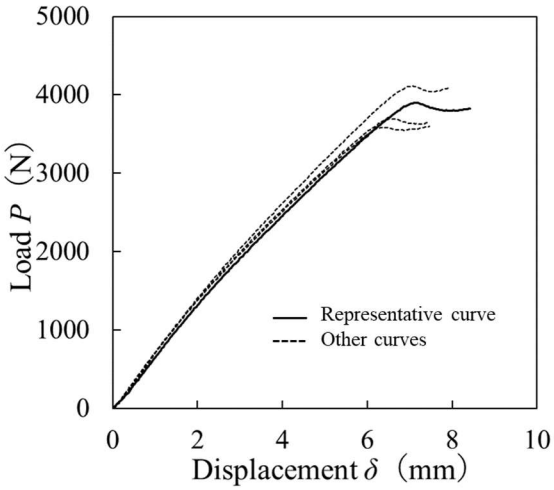

Fig. 3.4 Load–displacement curve for ENF test.

Initially, the load increased linearly with displacement, and the slope of the load–displacement curve decreased as the fracture process zone (FPZ) developed. At the maximum of the load–displacement curve, the FPZ was fully developed and crack propagation occurred. Subsequently, the cracks propagated further as the load decreased.

This load–displacement curve was used as fundamental data to obtain the *R*-curve.

3.3.3 Data reduction scheme of CBBM

In the ENF tests of adhesively bonded joints, crack length identification is difficult because of the formation of an FPZ with microcracks ahead of the crack tip. To overcome this, a data reduction scheme based on the concept of equivalent crack length, called the compliance-based beam method (CBBM), has been proposed [4-5], which depends only on the compliance of the specimen during testing. The outline of this data-reduction scheme is as follows: Based on the Timoschenko beam theory, the compliance of the ENF specimen, $C = \delta/P$, is given by:

$$C = \frac{3a^3 + 2L^3}{8E_f Bh^3} + \frac{3L}{10G_{13}Bh}, \tag{3.10}$$

where δ is the applied displacement and P is the applied load. B, h, and L are the dimensions of the specimen described in Fig. 3.3. E_f and G_{13} are the flexural modulus of the specimen and the shear modulus of the adherend, respectively. The material properties of CFRP are shown in Table 3.1. E_f can be obtained using Eq. 3.11, using the initial compliance C_0 and initial crack length a_0.

$$E_f = \frac{3a_0^3 + 2L^3}{8Bh^3 C_{0corr}}, \tag{3.11}$$

where C_{0corr} is given by

$$C_{0corr} = C_0 - \frac{3L}{10G_{13}Bh}. \tag{3.12}$$

Table 3.1 Mechanical properties of CFRP.

Young's modulus (GPa)			Poisson's ratio			Shear modulus (GPa)		
E_{11}	E_{22}	E_{33}	ν_{12}	ν_{13}	ν_{23}	G_{12}	G_{13}	G_{23}
130	9.9	9.9	0.31	0.26	0.21	4.0	4.0	7.5

During the crack propagation process, an FPZ was generated at the crack tip. The crack length used in Eq. 3.10 has been affected by the FPZ. Therefore, the real crack length a was replaced by the effective crack length a_e which included the effect of the FPZ. Combining Eqs. 3.10 and 3.11 yields:

$$a_e = a + \Delta a_{FPZ} = \left[\frac{C_{corr}}{C_{0corr}} a_0^3 + \frac{2}{3}\left(\frac{C_{corr}}{C_{0corr}} - 1\right) L^3\right]^{1/3}, \tag{3.13}$$

where C_{corr} is given by:

$$C_{corr} = C - \frac{3L}{10 G_{13} B h}. \tag{3.14}$$

Note that C_{0corr} is the correction factor for compliance C_0 at the initial crack length a_0, and C_{corr} is the correction factor for compliance C at crack length a. The energy release rate under mode II condition can be obtained using the Irwin–Kies relation, as:

$$G_{II} = \frac{P^2}{2B}\frac{dC}{da} = \frac{9P^2 a_e^2}{16 B^2 h^3 E_f}. \tag{3.15}$$

3.3.4 *R*-curve

Based on the load–displacement curve shown in Fig. 3.4, the *R*-curve obtained according to the CBBM method is displayed in Fig. 3.5 (a). The energy release rate along the vertical axis was calculated using Eq. 3.15, and the equivalent crack length on the horizontal axis was calculated using Eq. 3.13.

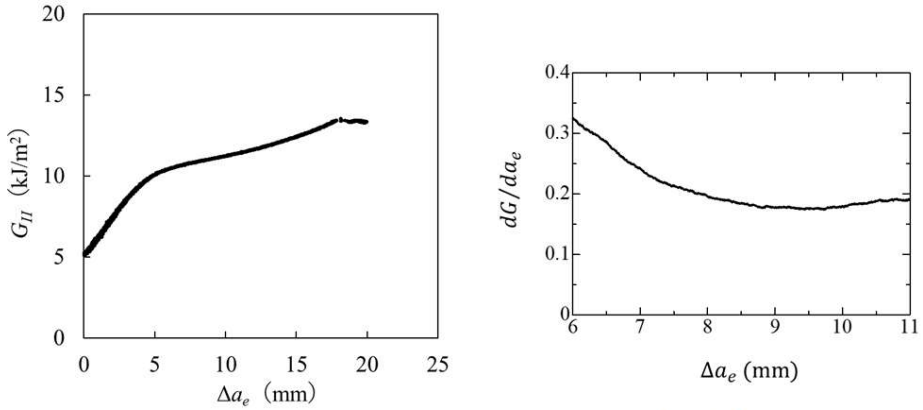

(a) *R*-curve. (b) dG/da_e vs. Δa_e.

Fig. 3.5 *R*-curve under mode II loading condition.

The profile of the *R*-curve is summarized as follows.

(1) In the first stage as shown in Fig. 3.5 (a), the initial increasing tendency occurring in the range $0 \leq \Delta a_e \leq 5\text{mm}$ reproduces the FPZ development.

(2) In the second range $5 \leq \Delta a_e \leq 15\text{mm}$, the slope of the *R*-curve is gentle.

(3) In the third range, the slight upward trend observed in the region $16 \leq \Delta a_e \leq 18\text{mm}$ is explained by the influence of the applied load as the crack approaches the central region of the specimen.

The critical energy release rate is generally defined as the value at which the energy release rate remains constant with respect to crack length. However, in some cases, the energy release rate was not constant for crack growth, as shown in Fig. 3.5 (a). In this case, the critical energy release rate is adopted as the value at which the slope of the *R*-curve is minimized [6]. Therefore, as shown in Fig. 3.5 (b), the energy release rate was differentiated with respect to the equivalent crack length to obtain the minimum slope. The energy release rate corresponding to dG/da_e become the minimum value was regarded as the critical energy release rate.

3.3.5 Mode I fracture toughness

In the case of Mode I condition, the *R*-curve can be easily obtained by using conventional DCB test. Because in Mode I, the crack tip is easily observed and the crack propagates stably. The *R*-curve under the Mode I condition is shown in Fig. 3.6 [7]. Note that the DCB specimen was same adhesive joint as in the ENF test in this chapter. As shown in this figure, the energy release rate is approximately constant irrespective as crack length. Therefore, the critical energy release rate for the Mode I condition can be defined by averaging the energy release rate during stable crack propagation in the range $10 \leq \Delta a \leq 25\text{mm}$.

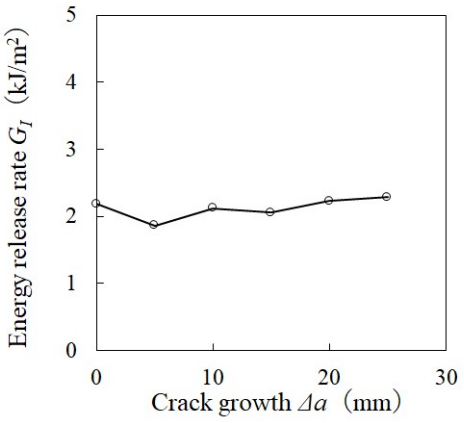

Fig. 3.6 *R*-curve under mode I loading condition.

In the case of the adhesive joints used ductile adhesive, the energy release rate in the plateau region of the *R*-curve was considered as the critical energy release rate value.

3.4 Determination of mixed-mode fracture criteria

To estimate the strength of adhesive joints using the CZM, a failure criterion under mixed-mode conditions is required, in addition to the mode I and II critical energy release rate values. In this study, the two criteria expressed in Eqs. 3.16 and 3.17 were determined under various mixed-mode conditions provided in the previous study [7].

The linear failure criteria can be defined as:

$$\frac{G_I}{G_{Ic}} + \frac{G_{II}}{G_{IIc}} = 1, \qquad (3.16)$$

The power-law failure criteria can be defined as:

$$\left(\frac{G_I}{G_{IC}}\right)^n + \left(\frac{G_{II}}{G_{IIC}}\right)^n = 1, \qquad (3.17)$$

Figure 3.7 (a) shows the experimentally obtained total energy release rate, $G_T = G_I + G_{II}$, as a function of the mode ratio, $m = G_{II}/G_T$ (refer to [7]), along with the corresponding calculations using the linear fracture model $(n = 1.0)$ and the power-law model $(n = 1.8)$. Figure 3.7 (b) shows the failure envelope between G_I/G_{IC} and G_{II}/G_{IIC}. From these figures, it was found that the power-law model accurately describes the mixed-mode failure criteria, whereas the linear model exhibits a significant prediction error (e.g., the error in G_T at $m = 0.8$ was as large as 25% of the experimental result). This implies that a power-law fracture model with $n = 1.8$ is suitable for this adhesive.

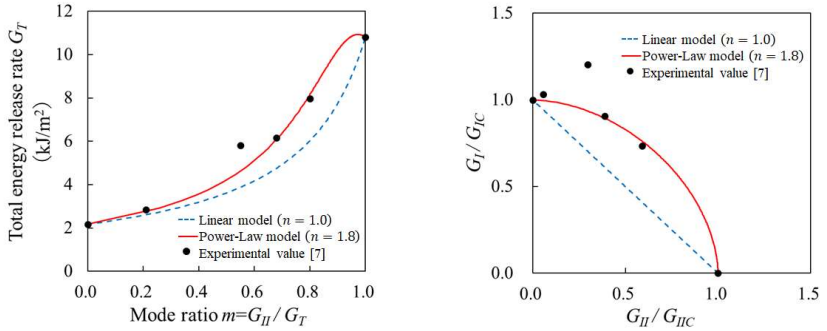

(a) Numerical and experimental steady-state total strain energy release rate vs. mode ratio.

(b) G_{mI}/G_{IC} vs. G_{mII}/G_{IIC}

Fig. 3.7 Comparison of numerical and experimental total strain energy release rate in plateau region.

3.5 CZM FE simulation of mixed-mode fracture of adhesively bonded joints

3.5.1 Cohesive damage model based on linear failure criterion

FE simulations were performed to verify the accuracy of the CZM in predicting mixed-mode fractures in adhesively bonded joints. CZM FE simulations were performed using the power-law-type model (Eq. 3.17) and Campilho's linear model (Eq. 3.16), respectively.

First, the well-known Campilho's CZM framework is briefly summarized. Figure 3.8 shows trapezoidal cohesive damage model proposed by Campilho et. al [8]. The behavior of the adhesive was integrated into the cohesive damage law and inserted into the trapezoidal cohesive damage model.

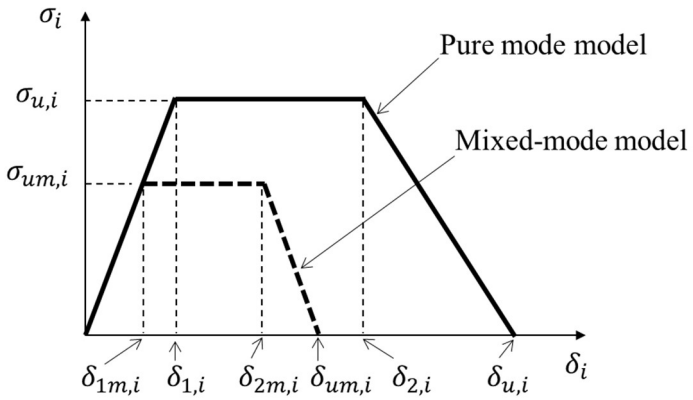

Fig. 3.8 Trapezoidal softening law for pure and mixed-mode cohesive damage models [8].

In the pure mode model, the area circumscribed by the trapezoid is equal to the critical energy release rate G_{iC} $(i = I, II)$ for each mode. Before damage onset, the following equation holds between the traction and separation for each mode.

$$\sigma_i = e_i \delta_i \quad (i = I, II). \tag{3.18}$$

Here σ_i, δ_i, and e_i $(i = I, II)$ are the stress, the relative displacement, and the stiffness parameter in each mode, respectively. In the mixed-mode model, damage onset is described by the following quadratic stress criterion.

$$\left(\frac{\sigma_I}{\sigma_{u,I}}\right)^2 + \left(\frac{\sigma_{II}}{\sigma_{u,II}}\right)^2 = 1\,, \tag{3.19}$$

where $\sigma_{u,i}\ (i = I, II)$ represents the local strength in each mode for the pure mode model. Considering Eqs. 3.18 and 3.19, the following equation is obtained for the displacement at damage onset.

$$\left(\frac{\delta_{1m,I}}{\delta_{1,I}}\right)^2 + \left(\frac{\delta_{1m,II}}{\delta_{1,II}}\right)^2 = 1, \qquad (3.20)$$

where $\delta_{1,i}$ and $\delta_{1m,i}\ (i = I, II)$ are the relative displacements in each mode corresponding to the damage initiation for the pure mode and mixed-mode, respectively. Subsequently, the equivalent mixed-mode displacement is defined as:

$$\delta_m = \sqrt{\delta_I^2 + \delta_{II}^2}\,, \qquad (3.21)$$

and mixed-mode ratio $\beta_i\ (i = I, II)$ is defined as the relative displacement:

$$\beta_i = \frac{\delta_i}{\delta_I}\,. \qquad (3.22)$$

The mixed-mode relative displacement at the onset of the damage δ_{1m} and the corresponding relative displacement for each mode $\delta_{1m,i}\ (i = I, II)$ are given as:

$$\delta_{1m} = \delta_{1,I}\delta_{1,II}\sqrt{\frac{1+\beta_{II}^2}{\delta_{1,II}^2 + \beta_{II}^2\delta_{1,I}^2}}\,, \qquad (3.23)$$

$$\delta_{1m,i} = \frac{\beta_i \delta_{1,\mathrm{I}}\delta_{1,\mathrm{II}}}{\sqrt{\delta_{1,\mathrm{II}}^2 + \beta_{\mathrm{II}}^2\delta_{1,\mathrm{I}}^2}}\,. \qquad (3.24)$$

Because a quadratic relative displacement criterion similar to that in Eq. 3.20 holds at the onset of the softening process, the mixed-mode relative displacement at the stress softening onset δ_{2m} and the corresponding relative displacement for each mode $\delta_{2m,i}\ (i = I, II)$ are obtained as:

$$\delta_{2m} = \delta_{2,I}\delta_{2,II}\sqrt{\frac{1+\beta_{II}^2}{\delta_{2,II}^2+\beta_{II}^2\delta_{2,I}^2}}, \tag{3.25}$$

$$\delta_{2m,i} = \frac{\beta_i\delta_{2,I}\delta_{2,II}}{\sqrt{\delta_{2,II}^2+\beta_{II}^2\delta_{2,I}^2}}. \tag{3.26}$$

The energy release rate in each mode at complete failure, G_i $(i = I, II)$, can be obtained from the area of the trapezoid shown in Fig. 3.8, as:

$$G_i = \frac{\sigma_{um,i}}{2}\left(\delta_{2m,i} - \delta_{1m,i} + \delta_{um,i}\right), \tag{3.27}$$

where $\sigma_{um,i}$ and $\delta_{um,i}$ $(i = I, II)$ are the maximum stress and the relative displacement at which complete failure occurs in modes I and II, respectively. Substituting Eq. 3.27 into the linear fracture criterion in Eq. 3.16, the ultimate mixed-mode relative displacement δ_{um} and the corresponding relative displacement for each mode $\delta_{um,i}$ $(i = I, II)$ are derived as:

$$\delta_{um} = \frac{2G_{IC}G_{IIC}(1+\beta_{II}^2) - \delta_{1m}(\delta_{2m}-\delta_{1m})(e_IG_{IIc}+\beta_{II}^2e_{II}G_{Ic})}{\delta_{1m}(e_IG_{IIc}+\beta_{II}^2e_{II}G_{Ic})}, \tag{3.28}$$

$$\delta_{um,i} = \beta_i\frac{2G_{IC}G_{IIC}(1+\beta_{II}^2) - \delta_{1m}(\delta_{2m}-\delta_{1m})(e_IG_{IIc}+\beta_{II}^2e_{II}G_{Ic})}{\delta_{1m}\sqrt{1+\beta_{II}^2}(e_IG_{IIc}+\beta_{II}^2e_{II}G_{Ic})}. \tag{3.29}$$

3.5.2 Cohesive damage model based on power-law criterion

For the power-law fracture criterion, Eq. 3.17, the same trapezoidal CZM modeling framework as that of the linear criterion is provided in Eqs. 3.18–3.26. Substituting Eqs. 3.22 and 3.27 into Eq. 3.17, the power-law criterion for the trapezoidal CZM is derived as:

$$\left\{\left(\frac{e_I\delta_{1m,I}}{2G_{Ic}}\right)^n + \left(\frac{e_{II}\beta_{II}^2\delta_{1m,I}}{2G_{IIc}}\right)^n\right\}\left(\delta_{2m,I} - \delta_{1m,I} + \delta_{um,I}\right)^n = 1. \tag{3.30}$$

Thus, from Eqs. 3.21 and 3.30, δ_{um} and $\delta_{um,i}$ for power-law criterion are given by:

$$\delta_{um} = (1+\beta_{II}^2)\left\{\frac{1}{\left(\frac{e_I\delta_{1m}}{2G_{IC}}\right)^n + \left(\frac{e_{II}\beta_{II}^2\delta_{1m}}{2G_{IIC}}\right)^n}\right\}^{\frac{1}{n}} - \delta_{2m} + \delta_{1m}, \qquad (3.31)$$

$$\delta_{um,i} = \beta_i\left[\sqrt{1+\beta_{II}^2}\left\{\frac{1}{\left(\frac{e_I\delta_{1m}}{2G_{IC}}\right)^n + \left(\frac{e_{II}\beta_{II}^2\delta_{1m}}{2G_{IIC}}\right)^n}\right\}^{\frac{1}{n}} + \frac{\delta_{1m}-\delta_{2m}}{\sqrt{1+\beta_{II}^2}}\right]. \qquad (3.32)$$

Note that the traction–separation behaviors predicted by the linear and power-law fracture models were the same up to the onset of softening, and the difference appeared only in the softening process.

3.5.3 Damage evolution in CZM

For the trapezoid in Fig. 3.8, the damage parameter d_m is determined.
in the plateau region of the trapezoid,

$$d_m = 1 - \frac{\delta_{1,m}}{\delta_m}, \qquad (3.33)$$

in the stress softening part,

$$d_m = 1 - \frac{\delta_{1,m}(\delta_{u,m}-\delta_m)}{\delta_m(\delta_{u,m}-\delta_{2,m})}, \qquad (3.34)$$

where δ_m is the current relative displacement, $\delta_{1,m}$ and $\delta_{2,m}$ are the first and second inflection points of the trapezoid. The maximum relative displacement $\delta_{u,m}$ is the displacement at which complete failure occurs. The softening behavior after the damage evolution defined in Eq. 3.34 can be expressed as:

$$\sigma_i = (1-d_i)e_i\delta_i \quad (i = I, II). \qquad (3.35)$$

When the linear fracture criterion is employed, the damage parameter is expressed as a function of δ_{1m}, δ_{2m} and δ_{um} (see Eqs. 3.23, 3.25, 3.28). In the case of the power-law criterion, δ_{1m} and δ_{2m} are expressed the same equations as linear fracture criterion, and δ_{um} is given by Eq. 3.31.

Thus, when the coordinates of each point of the trapezoid under mixed modes and the relationship between the equivalent displacement and damage variable are determined, the damage evolution can be predicted. Specifically, for the case of using the linear fracture criterion, several CZM FE simulations of the fracture process of adhesive joints under mixed modes have been published, where they employed a user-defined subroutine [9-13].

Instead of writing the subroutine, the FE analysis software ABAQUS allows us to perform the CZM simulation using damage datasets in tabular form, which comprises the damage variables and relative displacements after damage initiation for each mode ratio m. The mode ratio, defined by the energy release rate $m = G_{II}/G_T$, in Eq. 3.36 is written as a function of the stiffness e_I, e_{II} and the mixed-mode ratio β_{II}.

$$m = \frac{e_{II}\beta_{II}^2}{e_I + e_{II}\beta_{II}^2}. \qquad (3.36)$$

In the present simulation, the damage data from m = 0 (pure mode I) to m = 1 (pure mode II) for every mode ratio of 0.1, i.e., m = 0, 0.1, 0.2, …, and 1, were prepared in a tabular input file. The damage data for a given mode ratio were automatically calculated via interpolation using the ABAQUS software.

3.6 CZM FE modeling

To estimate the damage evolution behavior in the mixed-mode CZM, it is necessary to determine the traction–separation trapezoids under mode I and II loadings.

The load–displacement curves for these specimens were estimated based on the following boundary conditions. In a previous study, the DCB specimen shown in Fig. 3.9 was used for mode I fracture toughness tests [7], and its FE model is illustrated in Fig. 3.10 (a). The specimen arms were modeled using plane strain 4-node quadrilateral shell elements (CPE4: ABAQUS). The adhesive layer was modeled using 4-node cohesive elements (COH2D4: ABAQUS), including a trapezoidal cohesive damage model. The FE model for the DCB test comprised a combination of rigid beams and links that reproduced the experimental test. The displacements of the upper and lower arms were applied through links.

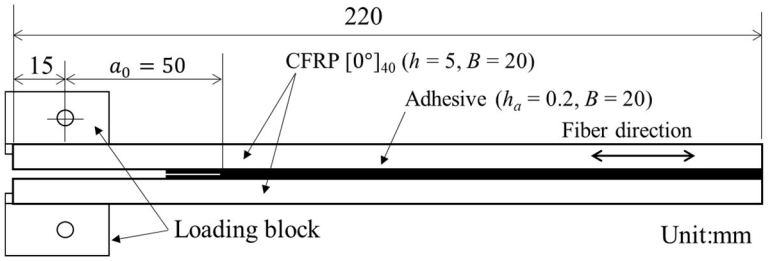

Fig. 3.9 Shape and sizes of adhesively bonded DCB specimen [7].

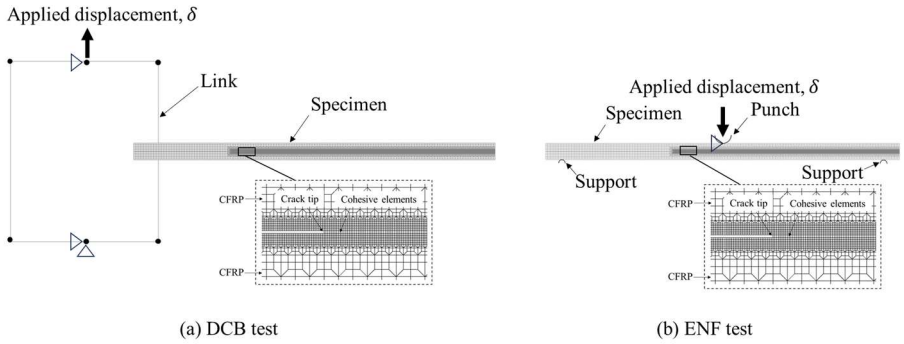

Fig. 3.10 Boundary conditions and mesh patterns for FE analysis for DCB and ENF specimens.

Fig. 3.10 (b) shows the FE model for the ENF test. The specimen was modeled using plane strain 4-node quadrilateral shell elements (CPE4: ABAQUS). The adhesive layer was modeled using 4-node cohesive elements (COH2D4: ABAQUS), including a trapezoidal cohesive damage model. The ENF specimen was subjected to a three-point bending loading, as shown in Fig. 3.10 (b). The loading cylinder and support are defined based on the geometry of the circular arc. For the contact between the arc curve and the mesh, Coulomb friction of $\mu = 0.1$ was assumed.

The traction–separation trapezoids were determined such that the area bounded by them matched the energy release rates in the plateau region of the *R*-curves of the DCB and ENF tests for modes I and II, respectively. Under the above constraint, the maximum tractions, $\sigma_{u,I}$ and $\sigma_{u,II}$, were determined iteratively such that the load–displacement curves calculated by the CZM FE simulation produce the best fit to the corresponding

experimental results in the DCB and ENF tests.

The determined traction–separation trapezoids for pure modes I and II are illustrated in Fig. 3.11. The CZM parameters of modes I and II are listed in Table 2. Figs. 3.12 (a) and (b) display the calculated and experimental load–displacement curves for the mode I and mode II tests, respectively. As shown in these figures, the predicted load–displacement curves agree well with the experimental curves for both the DCB and ENF tests, and the differences in the peak load values between the calculation and the corresponding experiment are less than 2%.

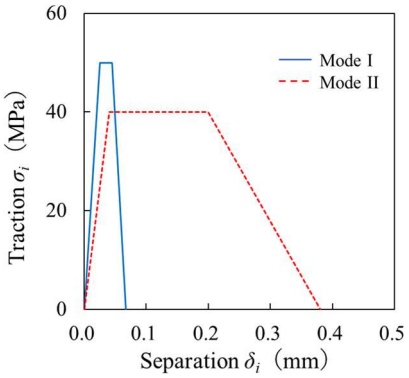

Fig. 3.11 Traction–separation laws for pure mode I and II loading conditions.

Table 2 CZM parameters under pure modes I and II.

Mode i	e_i (MPa/mm)	$\sigma_{u,i}$ (MPa)	G_{iC} (kJ/m^2)
I	2×10^3	50	2.17
II	1×10^3	40	10.8

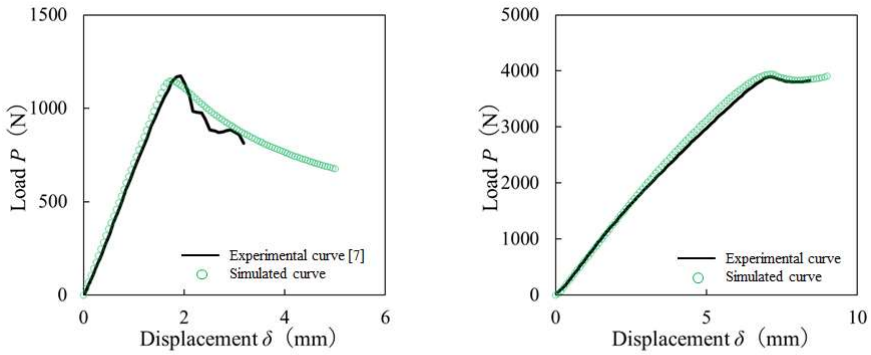

(a) DCB specimen (b) ENF specimen

Fig. 3.12 Comparison of numerical and experimental load-displacement curves for DCB and ENF specimens.

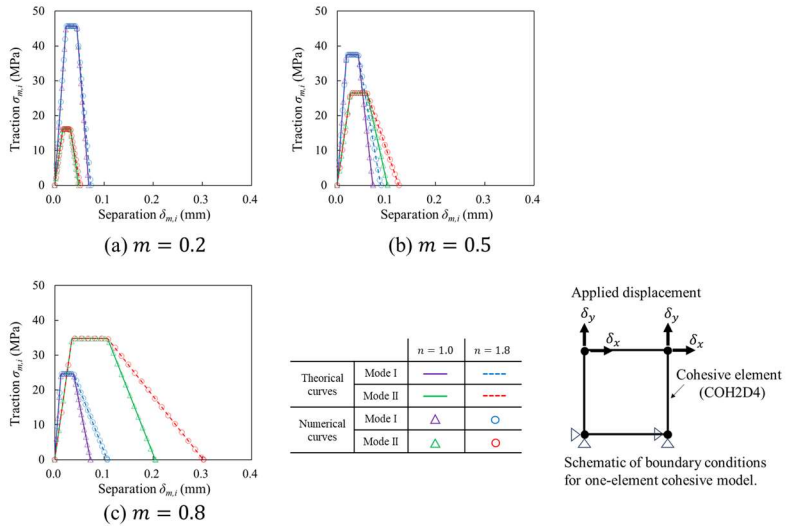

Fig. 3.13 Comparison of traction–separation curves derived from the theoretical equations and those obtained from one-element CZM FE calculations under various mixed-mode conditions.

To confirm the validity of the cohesive model using the tabular damage input file, a simple FE analysis using a one-element FE model was conducted under several mixed-mode conditions. The analytical model is illustrated in Fig. 3.13. A simple cohesive element corresponding to the adhesive layer was modeled using 4-node cohesive element (COH2D4: ABAQUS). The CZM parameters listed in Table 2 were used in the FE model. The displacements of the two lower-side nodes were constrained, while displacements δ_X and δ_Y were applied to the two upper-side nodes in the X and Y directions,

respectively. The relationship between δ_X and δ_Y was determined using Eq. 3.36 for a given mode ratio m.

The traction–separation curves obtained from the one-element FE calculation using the linear ($n = 1.0$) and power-law ($n = 1.8$) fracture models were compared with the theoretical curves under the three mixed-mode conditions $m = 0.2,\ 0.5$, and 0.8, as shown in Fig. 3.13. The results calculated using the one-element FE model agree well with the theoretical results irrespective of the fracture model and mixed mode. Therefore, the FE analysis with tabular-form input data for 11 discrete mode ratios (m = 0, 0.1, 0.2, …, 1) is sufficiently accurate.

3.7 CZM FE simulation and discussion

The CZM FE model for the mixed-mode F-S DCB is shown in Fig.3.14. This model had the same boundary conditions as those in a previous study [7]. The analytical procedure is described as follows.

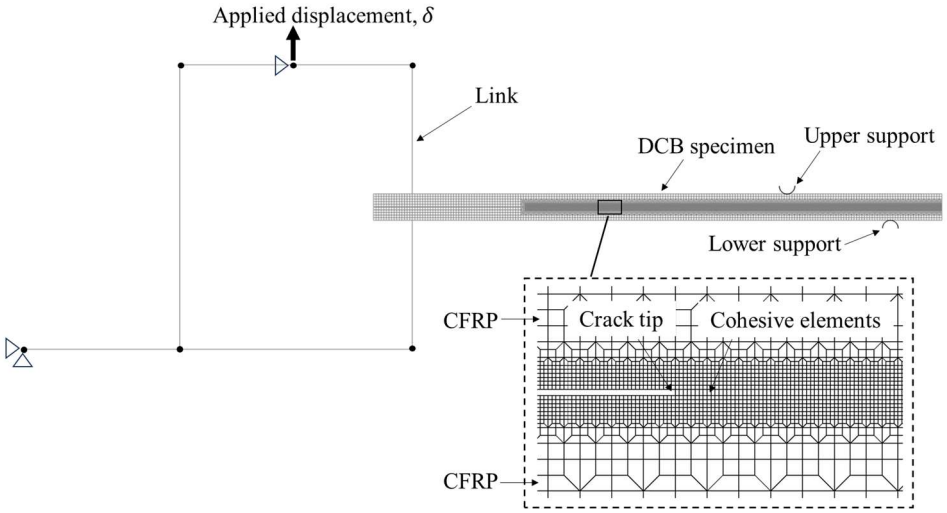

Fig. 3.14 Boundary conditions and mesh pattern for FE analysis for mixed-mode F-S DCB.

The adherends were modeled using 4-node plane strain shell elements (CPE4: ABAQUS), and the adhesive layer was modeled using 4-node cohesive elements (COH2D4: ABAQUS). Loading jigs featuring a mechanical link that allowed mixed-mode conditions were modeled using a combination of beams and links. The mode ratio is calculated using the distance between the nodes of the beam elements corresponding to the length of the arm of the links in the experiment. In the CZM FE simulation, the beam with upper and lower supports was subjected to a fixture displacement δ, as shown in Fig. 3.14. The friction coefficient between adherend and support was set to $\mu = 0.1$. The

mechanical properties of the adherends used in this analysis are listed in Table 1, and the CZM parameters of the adhesive layer are summarized in Table 2. Viscosity was included in the cohesive elements to improve the convergence of the calculations; the viscosity parameter was set to 0.001. The simulations were performed using a linear model $(n = 1.0)$ and a power-law model $(n = 1.8)$ for mode ratios of $m = 0.21, 0.5, 0.68$ and 0.8.

Comparisons between the experimental load–displacement curves obtained in a previous study [7] and the CZM FE simulations under various mixed-mode conditions are shown in Fig. 3.15. Both the experimental and simulated load–displacement curves exhibit a peak load followed by a gradual decrease for both the linear and power-law models, irrespective of the mixed-mode conditions. The initial slopes of the estimated curves agree well with those of the experimental curves.

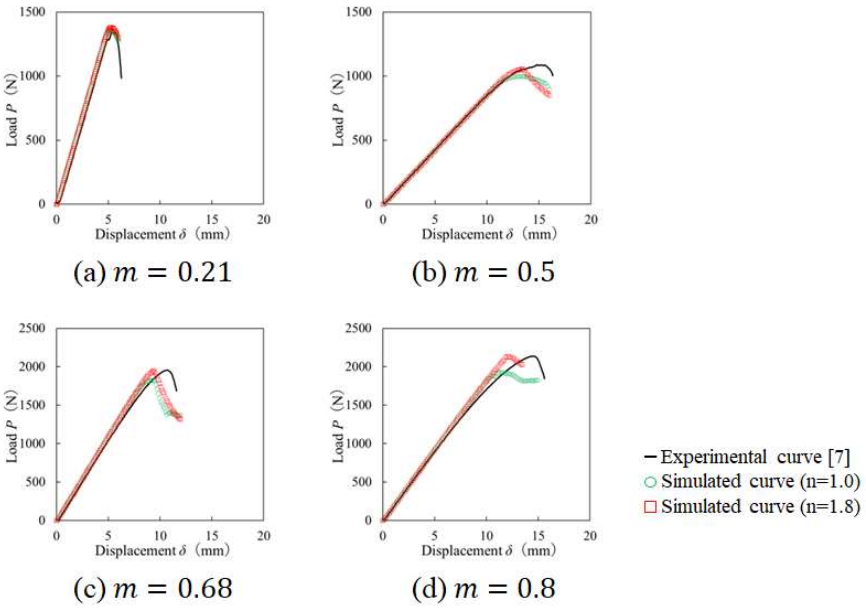

Fig. 3.15 Comparison of numerical and experimental load–displacement curves for various mixed-mode ratios.

Table 3 Peak loads in mixed-mode DCB experiments and the corresponding CZM FE simulations.

Mode ratio	Experiment Load (N)	Simulation ($n = 1.0$)		Simulation ($n = 1.8$)	
		Load (N)	$\frac{\text{Simulation}}{\text{Experiment}}$	Load (N)	$\frac{\text{Simulation}}{\text{Experiment}}$
0.21	1356	1359	1.002	1379	1.017
0.5	1087	996	0.916	1054	0.970
0.68	1957	1821	0.930	1948	0.995
0.8	2137	1926	0.901	2131	0.997

The peak loads calculated using the linear model $(n = 1.0)$ and the power-law model $(n = 1.8)$, along with the experimental results, are summarized in Table 3. In this table, the ratio of the simulated to the experimental loads is indicated, wherein the ratio ranges from 0.901 to 1.002 for the linear fracture model ($n = 1.0$), and 0.970 to 1.017 for the power-law model ($n = 1.8$). The maximum error in the linear model was as high as 10%; however, it provided conservative estimates of the fracture load for the overall mode ratios. In comparison with the case using the linear model, the calculations using the power-law fracture criterion were closer to the experimental results (the maximum error was 3%). These results are directly related to the accuracy of the calculation of the energy release rate depending on the model, as shown in Fig. 3.7.

3.8 Conclusions

To investigate how accurately the CZM can predict the load–displacement curves in mixed-mode F–S DCB tests, FE CZM simulations were performed, where two types of fracture criteria, specifically, linear and power-law type models, were employed.

1. The fracture toughness value under mode II condition during stable crack propagation was defined at the minimum of dG/da_e in the *R*-curve which was obtained by CBBM.
2. A mixed-mode CZM using the power-law fracture criterion (Eqs. 3.30-3.32) was presented in this work, wherein the damage evolution was expressed by the trapezoidal model.
3. The traction–separation trapezoids of the cohesive elements were determined iteratively such that the load–displacement curves calculated by the CZM FE simulation provided the best fit to the corresponding experimental results in the DCB and ENF tests, under the constraint that the area bounded by the trapezoid was equal to the energy release rate in the plateau region of *R*-curve.
4. Using both fracture criteria, CZM FE simulations of the mixed-mode F-S DCB were conducted using ABAQUS software. The load–displacement curves calculated using the power-law fracture criterion are closer to the experimental results (the maximum errors in the peak load calculated using the power-law model were 3%, whereas they were 10% in the linear model). Consequently, it was concluded that nonlinear fracture modeling is vital for accurate strength analysis of mixed-mode adhesive joints.

Reference

[1] D.S. Dugdale. Yielding of steel sheets containing slits. J Mech Phys Solids. 1960; 8: 100-4.
https://doi.org/10.1016/0022-5096(60)90013-2

[2] G.I. Barrenblatt, Mathematical Theory of Equilibrium Cracks in Brittle Failure. Advan Appl Mech. 1962; 7: 55-129.
https://doi.org/10.1016/S0065-2156(08)70121-2

[3] Benzeggagh M.L., Kenane M. Measurement of mixed-mode delamination fracture toughness of unidirectional glass/epoxy composites with mixed-mode bending apparatus. Compos. Sci. Technol. 1996; 56 (4): 439-449.
https://doi.org/10.1016/0266-3538(96)00005-X

[4] de Moura MFSF, Campilho RDSG, Gonçalves JPM. Pure mode II fracture characterization of composite bonded joint. Int. J. Solids. Struc. 2009;46:1589–1595. https://doi.org/10.1016/j.ijsolstr.2008.12.001.

[5] de Moura MFSF, da Silva LFM, de Moura AB, Morais JJL. Equivalent crack based mode II fracture characterization of wood. Eng. Frac. Mech. 2006;73:987–993.
https://doi.org/10.1016/j.engfracmech.2006.01.004.

[6] Moreira RDF, Oliveira V, Silva FGA, Vilar F, de Moura MFSF. Mode II fracture toughness of carbon-epoxy bonded joints with femtosecond laser treated surfaces. Int. J. Mech. Sci. 2018;148;707–713. https://doi.org/10.1016/j.ijmecsci.2018.09.029.

[7] Kouno Y, Imanaka M, Hino R, Omiya M, Yoshida F, *R*-curve behavior of adhesively bonded composite joints with highly toughened epoxy adhesive under mixed mode conditions. Int. J. Adhes. Adhes. 2021:105,102762.
https://doi.org/10.1016/j.ijadhadh.2020.102762.

[8] Campilho RDSG, de Moura MFSF, Domingues JJMS. Using a cohesive damage model to predict the tensile behaviour of CFRP single-strap repairs. Int. J. Solids Struc. 2008;45:1497–1512. https://doi.org/10.1016/j.ijsolstr.2007.10.003.

[9] Sun C, Thouless MD, Waas AM, et al. Rate effects for mixed-mode fracture of plastically deforming, adhesively-bonded structures. Int. J. Adhes. Adhes. 2009;29:434–443. https://doi.org/10.1016/j.ijadhadh.2008.09.003

[10] Chaves FJP, de Moura MFSF, da Silva LFM, Dillard DA. Numerical validation of a crack equivalent method for mixed-mode I + II fracture characterization of bonded joints. Eng. Frac. Mech. 2013;107:38–47. https://doi.org/10.1016/j.engfracmech.2013.05.008.

[11] Wang Z, Xian G. Cohesive zone model prediction of debonding failure in CFRP-to-steel bonded interface with a ductile adhesive. Comp Sci Tech. 2022:230:109315.

https://doi.org/10.1016/j.compscitech.2022.109315.
[12] Carvalho UTF, Campilho RDSG. Application of the direct method for cohesive law estimation applied to the strength prediction of double-lap joint. Theor. Appl. Frac. Mech. 2016;85:140–148. https://doi.org/10.1016/j.tafmec.2016.08.018.
[13] Mottaghian F, Taheri F. Assessment of failure mechanism of double-strap 3D-FML adhesively bonded joints under tensile and compressive loadings using cohesive zone modelling approach. Comp. Struc. 2023;318;117078.
https://doi.org/10.1016/j.compstruct.2023.117078.

Chapter 4 Elastic plastic analysis of adhesive joints considering anisotropic and hydrostatic stresses

4.1 Introduction

For the use of adhesively bonded joints to expand, the reliability of joint strength based on stress analysis should be clarified. Therefore, it is important to determine the accurate stress distribution in the adhesive layer. The use of a proper material model that realistically describes the stress–strain responses of an adhesive is crucial. High-toughened adhesives (e.g., polyurethanes and rubber-modified epoxy) exhibit significant nonlinear stress–strain behavior. Hence, for an accurate stress analysis of adhesive joints, the nonlinearity of the materials should be considered.

For nonlinear stress analysis, hyper-elastic models such as the Ogden [1] and Mooney–Rivlin [2, 3] models have been used for ductile adhesives (i.e., polyurethanes). The elastic–plastic analysis using the von Mises (isotropic) yield criterion has been employed for epoxy adhesives [4, 5], where the effect of hydrostatic stress on plasticity was ignored. Although, some studies revealed that hydrostatic stress significantly affects the yield stress of epoxy adhesives [6-10].

According to these previous studies, the effect of hydrostatic stress on yield behavior is expressed using linear and exponent Drucker–Prager models [7-10]. What is important here is the method used to determine the yield criterion. A set of material parameters of the exponent Drucker–Prager model was primarily determined using stress–strain curves under simple tensile and shear loading conditions. However, the stress multiaxialities in these tests were relatively low (the hydrostatic stress was $1/3$ of the yield stress in uniaxial tension and zero in shear). The applicability of this model to the higher stress multiaxiality must be verified because many other scenarios have an extremely high stress multiaxiality of the adhesive layer, such as in the butt-joint tension and at the crack tip in the double cantilever beam (DCB) test.

One of the characteristics of the Drucker–Prager model is that it can express the realistic shear/tensile yield–stress ratio of adhesives (c.f., $1/\sqrt{3}$ in the von Mises model) through hydrostatic-stress-dependent modeling. Alternatively, the flexible shear–tensile stress ratio can also be described using the hydrostatic-stress-independent model of plasticity through anisotropy modeling (e.g., the Hill'48 model [11]).

This study aimed to clarify whether hydrostatic stress modeling is a key parameter for a highly toughened epoxy adhesive by performing finite element (FE) stress–strain analyses of bulk uniaxial tension, simple shear, and butt-joint tension using the exponent Drucker–Prager plasticity models. The Drager-Prager model describes the normal-shear strength ratio by the stress-triaxiality effect (by λ-parameter). However, it is also possible

by using an anisotropic (hydrostatic-stress independent) plasticity model, e.g., Hill'48 model. Therefore, interest of the study was whether the hydrostatic-stress dependent material modeling is necessary or not for the stress analysis of adhesive bonded joints, specifically for butt-joint tension with high stress-multiaxiality. In the field of plasticity, the Hill'48 yield criterion is the first anisotropic plasticity model, and it is most popular and still widely used for the stress-strain analysis in various industries. The anisotropic yield function is a hot topic even today in the plasticity world, thus after Hill'48 model, more sophisticated models were presented, e.g., Yld2000-2d model [12], 6th order stress polynomial model [13] and Bezier interpolation model [14]. However, the formulations of these models are rather complicated, which include a lot of material parameters, therefore the simplest Hill'48 model was used for the discussion of hydrostatic-stress effect in the analysis of adhesive joint. The FE simulation results were compared with the results of digital image correlation (DIC) experiments. Specifically, for the Drucker–Prager model, our further interest was whether a set of material parameters determined from the bulk uniaxial tension and simple shear test is sufficient for the analysis of extremely high-stress multiaxiality, i.e., butt-joint tension.

4.2 Yield condition

4.2.1 von Mises criterion

Prior to the study, some basic essentials of yield criteria for describing the nonlinearity of the stress-strain relationship are summarized. Von Mises yield criterion is called the shear strain energy criterion. This criterion is defined as the material yielding when the shear strain energy reaches critical value of the total strain energy in multiaxial stress field. The total strain energy is defined by Eq. 4.1.

$$U_0 = U_v + U_d = \frac{1-2\nu}{6E}(\sigma_1+\sigma_2+\sigma_3)^2 + \frac{1+\nu}{6E}\{(\sigma_1-\sigma_2)^2+(\sigma_2-\sigma_3)^2+(\sigma_3-\sigma_1)^2\} \qquad (4.1)$$

where U_0 is total strain energy, U_v is dilatational strain energy, and U_d is shear strain energy. Von Mises yield criterion is defined as the material yielding when the second term on the right side of Eq. 4.1, U_d reaches its limit value $(U_d = (1+\nu)\sigma_T^2/(3E))$. For this reason, von Mises yield criterion ignores the dilatational strain energy devoted to the volume change for materials. Therefore, von Mises yield criterion is not affected by the hydrostatic stress σ_m $(\sigma_m = (\sigma_1+\sigma_2+\sigma_3)/3)$. Von Mises yield criterion is

defined by Eq. 4.2.

$$F = q^2 = \frac{1}{2}\{(\sigma_1 - \sigma_2)^2 + (\sigma_2 - \sigma_3)^2 + (\sigma_3 - \sigma_1)^2\} = \sigma_T^2 \qquad (4.2)$$

where σ_T is the tensile yield stress.

4.2.2 The linear Drucker Prager criterion

Since the hydrostatic stress effects the yield stress for adhesive joints, the consideration of the hydrostatic stress is necessary. The yield criterion that account for hydrostatic stress includes a series of the Drucker Prager yield criterion. A simple modification of the von Mises criterion that includes hydrostatic stress sensitivity is the linear Drucker Prager criterion. The linear Drucker Prager criterion is defined as follows:

$$F = q - p\tan\beta - \mathrm{d} \qquad (4.3)$$

Here q and p are the equivalent stress and the hydrostatic pressure. The hydrostatic pressure can be also written by $p = -\sigma_m = -(\sigma_x + \sigma_y + \sigma_z)/3$ using hydrostatic stress σ_m. Where $\tan\beta$ and d are the slope and intercept of the linear yield surface in the $p - q$ stress plane. Where β is commonly referred to as the friction angle of the material.

4.2.3 The hyperbolic Drucker Prager criterion

The hyperbolic Drucker Prager criterion is defined as follows:

$$F = \sqrt{(d_0' - p_0\, tan\,\beta)^2 + q^2} - p\, tan\,\beta - d' = 0 \qquad (4.4)$$

σ_T is the tensile yield stress, d_0' is initial hardening parameter, d' is hardening parameter, and p_0 is the initial hydrostatic tensile strength of material.

4.2.4 The exponent Drucker Prager criterion

The exponential Drucker Prager criterion is defined as follows:

$$q^b = \lambda\sigma_T^2 - 3(\lambda - 1)\sigma_T\sigma_m \qquad (4.5)$$

where σ_T is the tensile yield stress, σ_m is the hydrostatic component of stress, and λ is the hydrostatic stress-sensitivity parameter, and b is the exponent. λ also means

anisotropic parameter depending on the test condition calculated using one of the equations from Eqs. 4.6 to 4.8.

$$\lambda = \frac{\sigma_C}{\sigma_T} \qquad (4.6)$$

$$\lambda = \frac{\sigma_C^2}{3\sigma_S^2} \qquad (4.7)$$

$$\lambda = \frac{3\sigma_S^2}{\sigma_T^2} \qquad (4.8)$$

where σ_c is the compression yield stress, and σ_s is the shear yield stress.

4.2.5 Case study of hydrostatic stress dependence

The yield surface for various yield criteria described above is shown as in Fig. 4.1. The various parameters used for yield conditions are used of Table 1. Arbitrary values have been set for convenience.

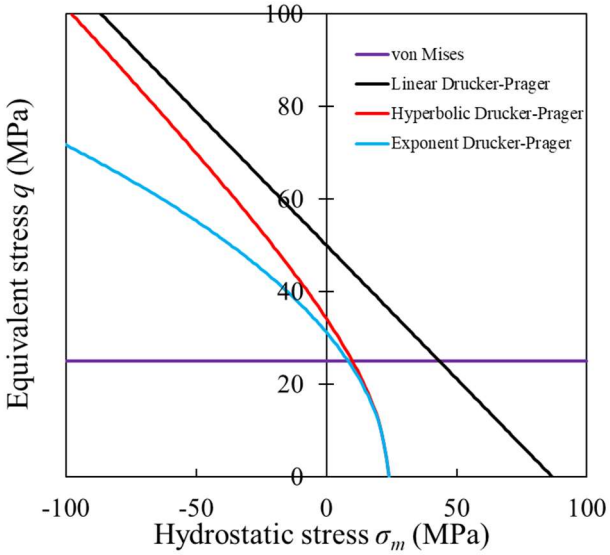

Fig. 4.1 Yield surface of the various criteria.

Table 1 Material properties for yield criteria.

β	$d = d'_0 = d'$	σ_T	σ_S	b
30°	50 (MPa)	25 (MPa)	18 (MPa)	2

In Fig. 4.1, von Mises criterion shows that the yield stress is independent of σ_m. The linear Drucker Prager criterion shows that the yield stress is linearly related to σ_m, indicating that the yield stress depends on the hydrostatic stress. The hyperbolic Drucker Prager criterion and the exponential Drucker Prager criterion have a nonlinear relationship between yield stress and σ_m, indicating that yield stress depends on hydrostatic stress. Therefore, a series of Drucker Prager criterion can be applied to the yield criterion of the adhesive while considering the hydrostatic stresses.

4.3 Evaluation of stress–strain curves of adhesive

4.3.1 Adhesive and adherend

In this study, the exponential Drucker-Prager model was selectively employed among above several models to evaluate adhesive yield stress. In this model, the hydrostatic stress-sensitivity parameter λ must be obtained as shown in Eq. 4.5. The parameter λ can defines the hydrostatic stress-sensitivity and anisotropy of the yield stress. Here, λ was defined by Eq. 4.8, because in practice, adhesive joints are used under tensile and shear stress conditions. Therefore, tensile and shear tests should be performed to obtain stress–strain curves of the adhesive. The tensile test and shear test were performed using bulk adhesive specimen and thick adherend shear test specimen (TAST). In addition, stress–strain curves were evaluated using butt joints to assess the validity of the exponential Drucker-Prager model under extremely high-stress multiaxiality condition. The adhesives and adherends used for these three types of specimens are as follows.

A rubber-modified epoxy adhesive film (AF163-2U, nominal thickness of 0.14 mm, 3M) was used for the bulk adhesive specimen, thick adherend shear test specimen (TAST), and the butt joint. The adherends of the TAST specimen and the butt joint were composed of mild steel (JIS.SS400).

4.3.2 Specimen manufacturing

The shapes and dimensions of the bulk adhesive specimens are shown in Fig. 4.2 (a). The adhesive films were stacked in 36 layers on the release-treated plate, which was placed in a vacuum bag for a few minutes to avoid air inclusions. Subsequently, it was

clamped between release-treated plates via 3 mm-thickness gauges and cured at 120 ℃ for 1 h. After cooling to room temperature, the bulk adhesive plate was trimmed into dumbbell-shaped specimens.

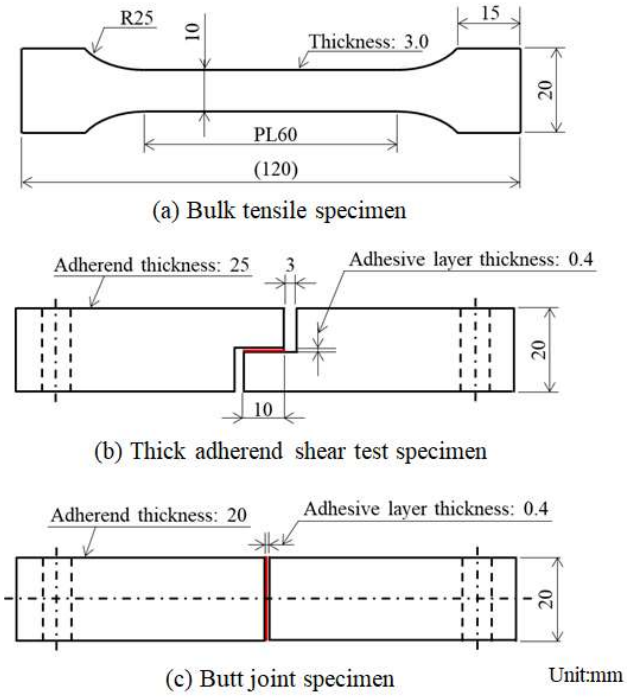

Fig. 4.2 Geometry of bulk tensile specimen (a), thick adherend shear test specimen (b) and butt joint specimen (c).

The shapes and dimensions of the TAST and joint specimens are shown in Figs. 4.2 (b) and (c), respectively. Prior to bonding, a teflon film with release agent was placed into SS400 except for the bonding surface. Even if spew fillets are formed, they can be easily removed from the adherend. The SS400 surfaces were polished with emery paper #120, and then the abrasive surfaces were cleaned with acetone to remove dust and oil. Four layers of the film adhesive were stacked using vacuum bagging to avoid air contamination. A spacer was used to control the thickness, resulting in a nominal value of 0.4 mm. The assembled joints were clamped using steel jigs to prevent them from slipping out of alignment and cured in the thermostatic chamber at 120 ℃ for 1 h. Adhesive excess on the sides of joints was removed with a file and emery paper.

4.3.3 Testing procedure

Tensile test of the bulk adhesive, TAST specimen, and butt joint was performed at controlled room temperature using a universal testing machine (AG-IS, Shimadzu)

equipped with a 50 kN load cell. The crosshead speed was 0.5 mm/min. The strain rate for bulk tensile test was $1.39 \times 10^{-4}\ (s^{-1})$ and for TAST and butt-joint tensile tests were $2.08 \times 10^{-2}\ (s^{-1})$. As the tensile tests were carried out with uniform crosshead speeds for the bulk adhesive specimen and the adhesively bonded joints, the strain rates of both were differed. The effect of strain rate on the maximum shear stress was investigated for the TAST tests; the maximum shear stress at $1.39 \times 10^{-4}\ (s^{-1})$ was 13% lower than that $2.08 \times 10^{-2}\ (s^{-1})$. The unified evaluation of strain rate is a subject for future research.

To obtain the stress–strain curves of the bulk adhesive, TAST specimen, and butt joint, the relative displacement between the measurement points on the specimen was measured using DIC and calculated the strain based on the displacement. The measurement points of the bulk adhesive were located 1 mm from the center of the specimen, and the points of the TAST and butt joints were located on the adherend in the vicinity of the respective adhesive layers. The details of these points are described in the following.

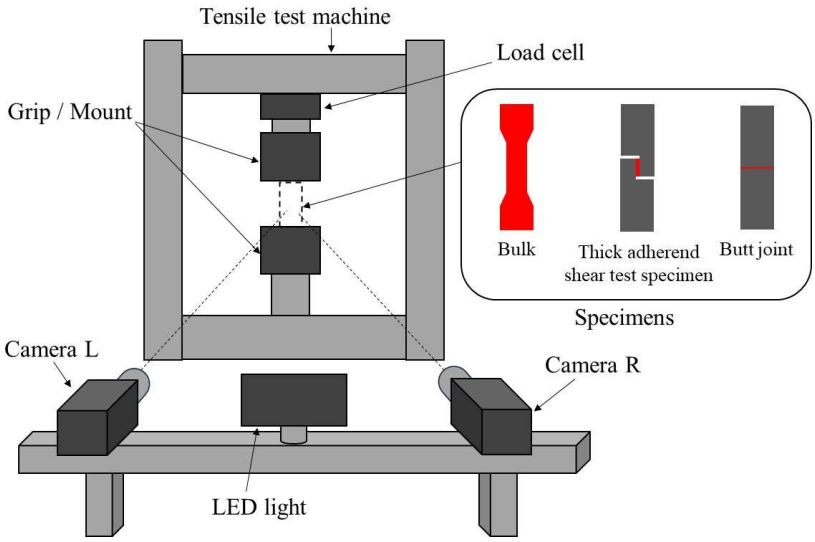

Fig. 4.3 Illustration of tensile test for bulk and adhesively bonded joints with full-field strain measurement using DIC system.

A schematic of the experimental configuration is shown in Fig. 4.3. The full-field displacements of the specimens were obtained using two separate cameras as shown in this figure. For synchronized recording with a sampling frequency of 1.0 Hz, both the

image pair and load cell signals were accumulated on a personal computer. Additionally, random speckle patterns were sprayed on the specimen surfaces to obtain accurate deformations. The DIC data were recorded using a machine vision camera (GS3-U3-51S5M-C, Point Grey Research) with a C-mount lens (Xenoplan 1.9/35, Schneider KREUZNACH), having a resolution of 2448×2049 pixels, and the pixel size was approximately 0.03 mm. Commercial DIC software (VIC-3D, Correlated Solutions) was used to measure the displacements.

4.4 Strain measurements for tensile and shear

A typical contour plot of the *Y*-direction displacement of a bulk adhesive specimen under tensile loading obtained by DIC analysis was shown in Figure 4.4. The *Y*-direction is defined as the tensile direction. In all the subsequent figures, the *Y*-direction is assumed to be the tensile direction. As the specimen was pulled in the *Y*-direction, the displacement at the top was greater than that at the bottom. The strain ε_Y of the bulk specimen was calculated by Eq.4.9. V_1 and V_2 are *Y*-directional displacements at points P_1 and P_2 in the center of the specimen. d is the initial distance between the points P_1 and P_2.

$$\varepsilon_Y = \frac{V_1 - V_2}{d} \qquad (4.9)$$

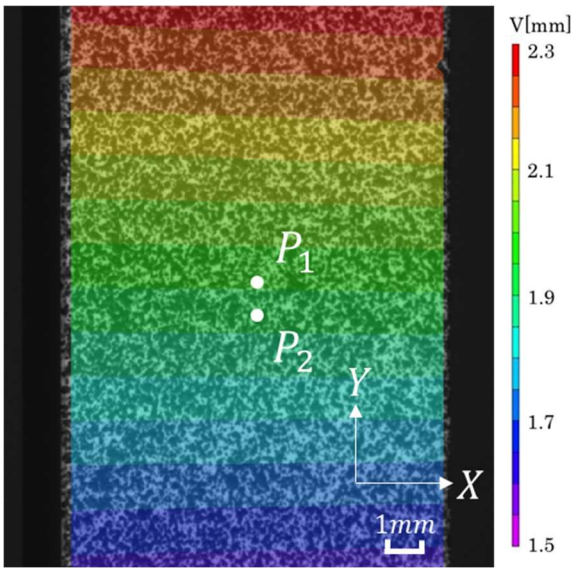

Fig. 4.4 Typical image of Y-directional displacement, V for bulk specimen.

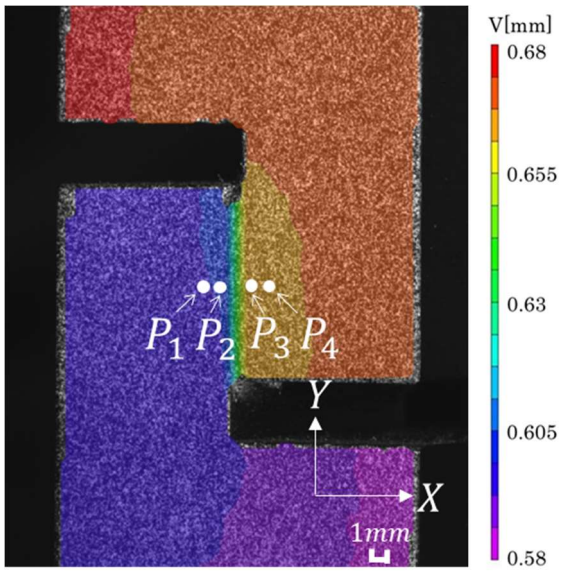

Fig. 4.5 Typical image of Y-directional displacement, V for thick adherend shear test specimen.

Figure 4.5 shows a typical contour image of the Y-directional displacement V near the adhesive layer of the TAST specimen. Any cracks were not identified from the DIC images within the measurement range of the stress-strain curve. The V distribution in the adhesive layer of the TAST specimens was almost uniform, except near the edges. The shear strain of the adhesive layer was calculated using the method described by Kosmann et al. [15]. To obtain the shear strain of the middle part of the adhesive layer, the Y-directional displacements V_1, V_2, V_3, V_4 at four points on the horizontal line of the left and right parts of the adherends, P_1, P_2, P_3, P_4 were measured across the adhesive layer in the center of the specimen. Here, the adherend to the left of the adhesive layer was described as adherend 1, and the adherend to the right as adherend 2. The distances between P_1 and P_2 and between P_3 and P_4 were defined as d_1 and d_2, respectively. The shear strain between P_1 and P_2 on adherend 1, γ_{adhe1}, and that γ_{adhe2}, were determined using the following equations.

$$\gamma_{adhe1} = \frac{V_2 - V_1}{d_1}, \qquad \gamma_{adhe2} = \frac{V_4 - V_3}{d_2} \tag{4.10}$$

The distance between P_2 and P_3 across the adhesive layer was defined as d_3. The relative displacement $V_3 - V_2$ between P_2 and P_3 consisted of the following three

components: the relative displacements in adherend 1, the adhesive layer, and adherend 2. Therefore, the shear strain of the adhesive layer, γ_{adhe}, was calculated by subtracting the first and third components of the relative displacement from $V_3 - V_2$ and dividing that by the thickness of the adhesive layer, t as expressed in the following equation.

$$\gamma_{adhe} = \frac{(V_3 - V_2) - 0.5\gamma_{adhe1}(d_3 - t) - 0.5\gamma_{adhe2}(d_3 - t)}{t} \qquad (4.11)$$

The normal stress–normal strain and shear stress–shear strain curves for the bulk adhesive specimens and TAST specimens are shown in Figs. 4.6 (a) and (b), respectively. Here, the normal stress is the respective loads divided by the cross-sectional area. The shear stress is the respective loads divided by the adhesive area of the TAST specimen. In Fig.4.6 (a), only two test pieces were tested for the bulk specimens due to the difficulty of manufacturing specimens, where slight bubbles and wrinkles were observed in the lower strength specimen, so the higher strength curve was adopted as the representative stress-strain curve. Figures 4.6 (a) and (b) show the clear yielding behavior under both tensile and shear loading, and the slope of the stress–strain curve after yielding was significantly reduced under both tensile and shear loading conditions.

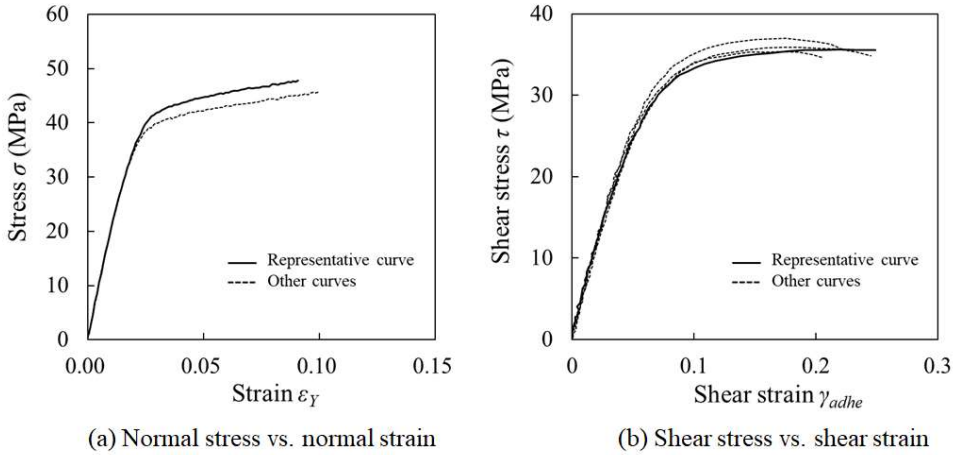

(a) Normal stress vs. normal strain (b) Shear stress vs. shear strain

Fig. 4.6 Experimental stress-strain curves obtained from bulk specimen (a) and thick adherend shear test specimen (b).

4.5 Determination of material parameters for the exponent Drucker–Prager model

4.5.1 Material parameters

The exponent Drucker–Prager criterion has been used to reproduce the behavior of toughened adhesives [7-10, 16]. This criterion is sensitive to the hydrostatic stress component, even with high stress values [7], and is adequate for analyzing many polymeric materials. The exponent Drucker–Prager criterion is defined as follows.

$$\sigma_e^b = \lambda\sigma_T^2 - 3(\lambda - 1)\sigma_T\sigma_m \qquad (4.12)$$

where σ_e is the effective von Mises stress, σ_T is the tensile yield stress, σ_m is the hydrostatic component of stress, and λ is the hydrostatic stress-sensitivity parameter, and b is the exponent. Here, λ is frequently calculated using one of the following equations, depending on the test condition for the modeling material.

$$\lambda = \frac{\sigma_C}{\sigma_T} \qquad (4.13)$$

$$\lambda = \frac{\sigma_C^2}{3\tau_Y^2} \qquad (4.14)$$

$$\lambda = \frac{3\tau_Y^2}{\sigma_T^2} \qquad (4.15)$$

where σ_C is the compression yield stress, τ_Y is the shear yield stress. In this study, λ was calculated using Eq. 4.15, which was obtained from the tensile and shear tests because adhesive-bonded joints are generally subjected to combined tensile and shear stresses.

The hardening rule was defined by a hardening curve representing the stress and plastic strain values obtained from the tensile test of the bulk adhesive. Figure 4.7 shows the hardening curve of the adhesive. Finally, the flow parameter Ψ, which is defined as the angle of dilation, is required for a high plastic strain behavior. The exponent Drucker–Prager criterion was implemented in ABAQUS as a plastic model [17], and it is expressed as follows:

$$aq^b = p + p_t \qquad (4.16)$$

where $q = \sigma_e$ and $p = -\sigma_m$. Comparing Eqs 4.12 and 4.16, the following equations

were obtained:

$$a = \frac{1}{3\sigma_T(\lambda - 1)} \qquad (4.17)$$

$$p_t = a\lambda\sigma_T^2 \qquad (4.18)$$

Because b is typically 2 for polymeric materials [7], $b = 2$ was used.
Subsequently, the flow parameter Ψ, was defined as the angle of dilation by the following equation.

$$tan\,\Psi = \frac{3(1 - 2\nu^p)}{2(1 + \nu^p)} \qquad (4.19)$$

where ν^p is the plastic component of Poisson's ratio.

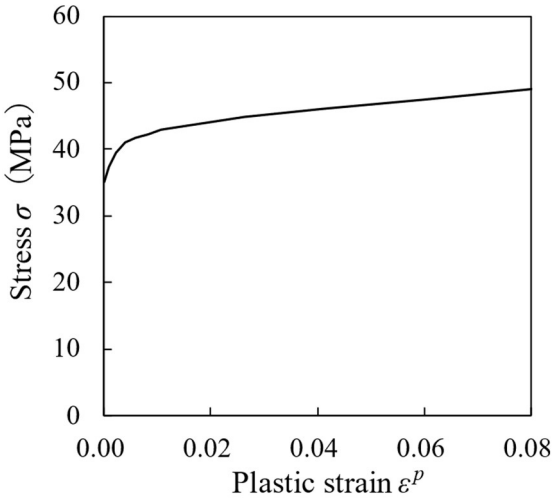

Fig. 4.7 Hardening curve obtained from tensile test of the bulk

4.5.2 Determination of the hydrostatic stress-sensitivity parameter λ

In order to define λ, σ_T and τ_Y must be obtained. In the plastic region, the longitudinal stress for tensile test σ and the shear stress for TAST τ are functions of the corresponding plastic strains ε^p and γ^p, respectively. From plasticity theory, σ_T and τ_Y should be determined based on the plastic-work conjugate pairs of (σ, ε^p) and (τ, γ^p) which satisfy the following equation.

$$w^p = \int \sigma d\varepsilon^p = \int \tau d\gamma^p \qquad (4.20)$$

For various values of plastic work w^p, σ_T and τ_Y were determined as σ and τ satisfying Eq. 4.20; subsequently, the parameter λ was calculated using Eq. 4.15. Figure 4.8 shows the relation between λ and w^p. As shown in this figure, initially, λ increased with increasing w^p, then converged to an almost constant value. In the finite element analysis (FEA) described below, this convergence value was used for λ.

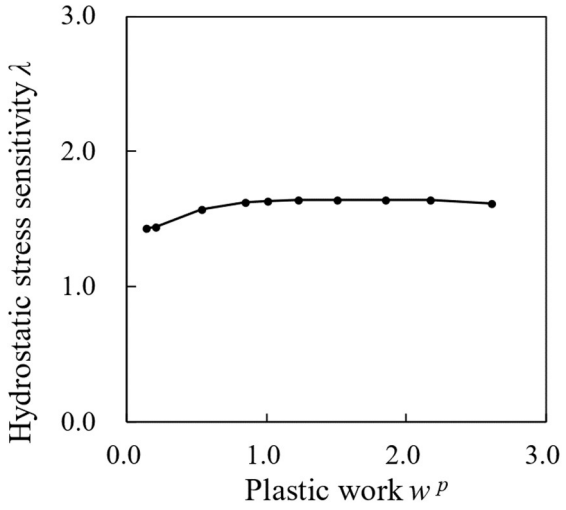

Fig. 4.8 Relationship between hydrostatic stress sensitivity parameter and plastic work.

4.5.3 Determination of the flow parameter Ψ

In order to define Ψ, the plastic component of Poisson's ratio ν^p must be obtained. Here, ν^p was obtained using the longitudinal strain, ε_T, transverse strain, ε_t, Young's modulus E, and elastic component of Poisson's ratio ν^e as follows:

$$\nu^p = \frac{-\varepsilon_t^p}{\varepsilon_T^p} \qquad (4.21)$$

$$\varepsilon_T^p = \varepsilon_T - \frac{\sigma}{E} \qquad (4.22)$$

$$\varepsilon_t^p = \varepsilon_t + \nu^e \frac{\sigma}{E} \qquad (4.23)$$

From these data, the plastic component of Poisson's ratio versus longitudinal plastic strain was constructed, as shown in Fig. 4.9. This figure shows that initially, ν^p decreased rapidly with increasing ε_T^p, then converged to an almost constant value. In the FEA described below, the angle of dilation for FEA was calculated from Eq. 4.19 using the converged value of the plastic component of Poisson's ratio.

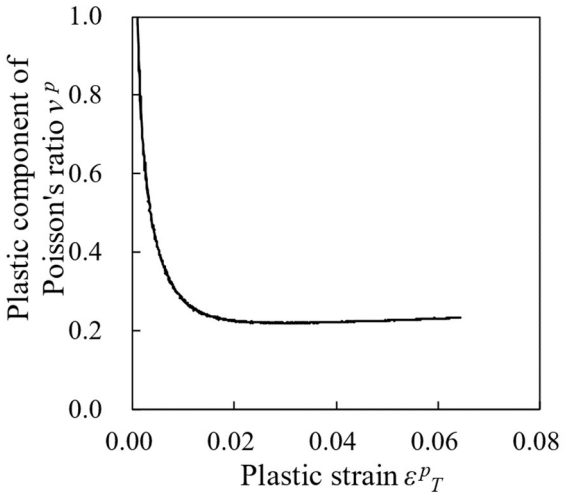

Fig. 4.9 Relationship between plastic component of Poisson's ratio and plastic strain.

4.5.4 Material parameters determination for the Hill'48 model

The exponential Drucker-Prager model can describe the anisotropy of yield stress by using hydrostatic sensitivity parameter λ. However, it is also possible by using another anisotropic (hydrostatic-stress independent) plasticity model. A typical anisotropic material model is the Hill'48 criterion [11], which is an extension of the von Mises yield criterion. The Hill'48 yield criterion is expressed as Eq. 4.24.

$$f(\sigma) = \frac{1}{2}\{F(\sigma_{22}-\sigma_{33})^2 + G(\sigma_{33}-\sigma_{11})^2 + H(\sigma_{11}-\sigma_{22})^2\}$$
$$+L\sigma_{23}^2 + M\sigma_{31}^2 + N\sigma_{12}^2 - \frac{1}{3}(F+G+H)\sigma_e^2 = 0 \qquad (4.24)$$

The anisotropy parameters *F*, *G*, *H*, *L*, *M*, and *N* were determined using the following procedure. Parameters *F, G* and *H* were set to 1 and *L* and *M* were 3 on the assumption that the anisotropy does not appear in normal stresses, and σ_{23} and σ_{31} shear stress components. Parameter *N*, which determines the anisotropy of normal to shear stress, was determined from Drucker-Prager's λ-parameter, such as $N = \sigma_T^2/\tau_Y^2 = 3/\lambda$.

4.6 Comparison of experimental and simulated stress–strain curves

4.6.1 FE models

To compare the experimentally obtained and simulated normal stress–normal strain curve of the bulk adhesive and shear stress–shear strain curve in the adhesive layer of the TAST specimen, the FE analysis of the bulk adhesive and TAST specimen under tensile loading was conducted. The FEA was performed using the ABAQUS standard, considering geometrical nonlinearity. The dependence of the modulus and hardening behavior on the strain rate was not included in the analysis. The material properties of the adhesive were determined using the exponent Drucker–Prager model. In addition, FEA utilizing the von Mises and Hill'48 model was conducted in the same manner to compare the adhesive yield stress. The material constants used for FEA are summarized in Tables 4.2 and 4.3.

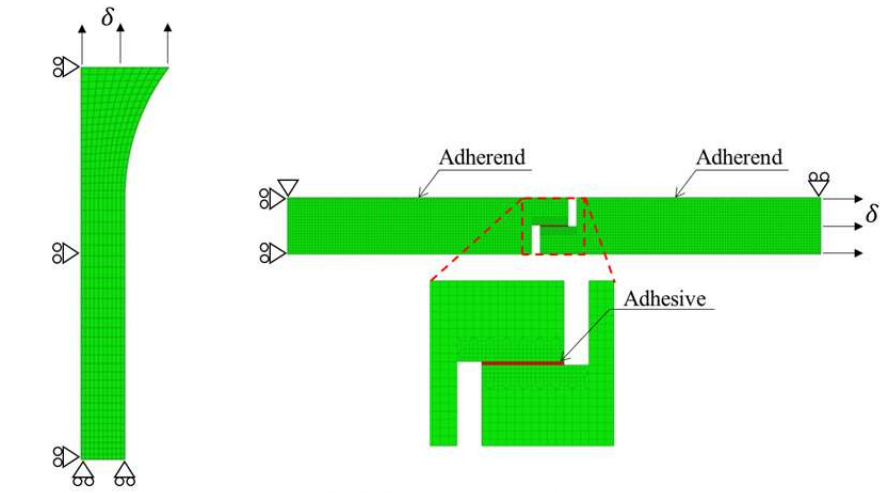

(a) Bulk specimen (b) Thick adherend shear test specimen

Fig. 4.10 Boundary conditions for bulk and thick adherend shear test specimens.

Table 4.2 Material properties based on exponent Drucker-Prager model.

E (GPa)	ν^e	λ	a (MPa^{-1})	ν^p	Ψ (°)	σ_T (MPa)
1775	0.38	1.639	0.0149	0.23	33.7	35.1

Table 4.3 Anisotropic parameters for Hill'48 model.

F	G	H	L	M	N
1	1	1	3	3	1.8

Figures 4.10 show the boundary conditions for the bulk and TAST specimens, where the bulk specimen was a 1/4 symmetric model, and the TAST specimen was the full model. The mesh sizes of the FE models for the bulk and TAST were used for 0.5 mm and 0.4 mm, respectively. It is recognized that bulk tensile model has adequate mesh sizes because stress concentration does not occur. The reason why TAST model used coarse

mesh is to improve the convergence of the nonlinear analysis. The shear stress in TAST was evaluated at the center of the adhesive layer, where stress was in a state of essentially uniform over the overlap, rather than at the end of the joint where stress concentration occurs. Stress was evaluated with coarser meshes and fine meshes in advance to confirm there have no difference. As shown in Figs. 4.10, uniform vertical and horizontal displacements were applied to the upper and right surfaces of the bulk and TAST specimens, respectively. Moreover, the vertical displacements of all nodes at the bottom and horizontal displacements of all nodes on the left side were constrained for the bulk specimen, whereas the horizontal displacements of all nodes on the left edge and vertical displacement of one node on the left corner were constrained for the TAST specimen. The bulk and TAST specimens were analyzed using four-node plane stress elements (CPS4, ABAQUS) and four-node plane strain elements (CPE4, ABAQUS), respectively.

4.6.2 Results of FEA

Figures 4.11 shows the representative experimentally obtained stress-strain curves for tensile test and shear test compared to simulated results. Simulation results involve the exponent Drucker–Prager, Hill'48, and von Mises models which were applied to the adhesive elements in FE model. In Fig. 4.11 (a), the experimental stress–strain curve under tensile conditions was consistent with the simulated curves from the exponent Drucker–Prager, Hill'48, and von Mises models. This was because the simulated curves were calculated using the same tensile plastic-hardening data as the input.

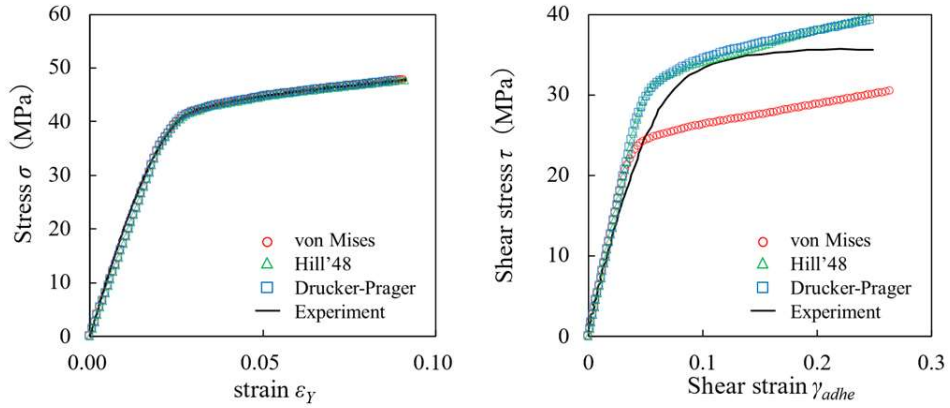

(a) Normal stress vs. normal strain (b) Shear stress vs. shear strain

Fig. 4.11 Comparison between simulation results and experimental data.

Subsequently, as shown in Fig. 4.11 (b), the yield stress under shear loading conditions simulated using the von Mises model was approximately 30% lower than the experimental yield stress, and the slope of the simulated stress–strain curve after yielding was greater than that of the experimental curve. When the experimental and simulated curves were compared using the Hill'48 and exponent Drucker–Prager model, the yield stress almost agreed with that of the experimental curve, whereas the difference was confirmed in strain hardening behavior between the experimental curve and the analysis curves. In this case, void formation or crack initiation were suspected, but these were not confirmed by DIC observation. Because the DIC captured images only on the surface but not bulk inside. Even if the damage evolution is neglected, it is not surprising that shear and tension have different hardening characteristics, because 'strain hardening is a unique function of the plastic strain (or plastic work)' is just a simple assumption which comes from metal plasticity theory, but it has not proven yet for polymers. Even for metallic plasticity, such stress-state dependent hardening behavior was recently observed, and discussed as 'anisotropic hardening' [18].

The yield stress estimated using the exponent Drucker–Prager model almost consistent with the experimental. Because the hydrostatic component of stress $\sigma_m = 0$ under shear stress condition, substituting this into the yield condition Eq. 4.16 of the exponent Drucker–Prager model, the following equation was obtained:

$$\sigma_e = \sqrt{\lambda}\sigma_T \qquad (4.25)$$

This equation implies that by multiplying the tensile yield stress estimated from the von Mises model by $\sqrt{\lambda}$, the obtained stress is equal to the experimental yield stress. Because the results of this operation were the same as those in the Hill'48 model, the estimated curves for the exponent Drucker–Prager model agreed with those of the Hill'48 model.

4.7 Estimation of stress–strain relation for the butt joint based on the exponent Drucker–Prager model

4.7.1 Experimental stress–strain curve for the butt joint

For accurate stress and strain analyses of a wider range of adhesive joints, it is necessary to investigate which model can be adapted to estimate the stress–strain curve of the adhesive layer, even when the stress multiaxiality of the adhesive layer is high, as in adhesively bonded butt joints. In this section, the stress–strain curves of the butt joints were estimated using the exponent Drucker–Prager and Hill'48 models.

To determine the stress–strain curve of the adhesive layer of the butt joint, the strain

of the adhesive layer from the relative displacement of the adherend near the adhesive layer was calculated using DIC, as in the case of the TAST specimen. Because the stress distribution in the adhesive layer of a butt joint is uniform, except near the edges [19], the strain in the adhesive layer was measured at the center of the butt joint.

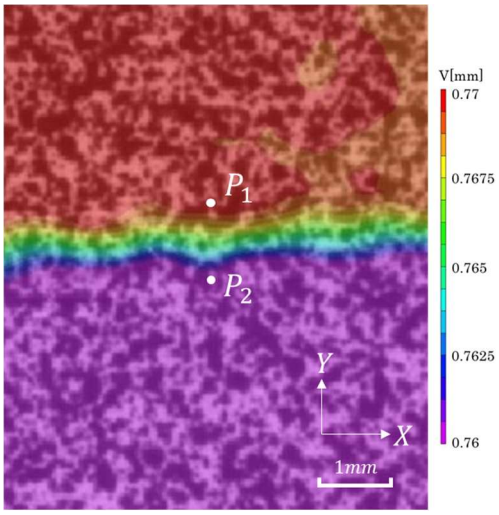

Fig. 4.12 Typical image of Y-directional displacement, V for butt joint.

Figure 4.12 shows a typical contour image of the y-directional displacement near the adhesive layer. The strain in the adhesive layer was calculated via the Eq. 4.26 using the Y-directional displacement V_1 at the P_1 point approximately 0.5 mm above the adhesive layer–upper adherend interface, the Y-directional displacement V_2 at the P_2 point approximately 0.5 mm below the adhesive layer–lower adherend interface, and the thickness t of the adhesive layer.

$$\varepsilon_{adhe} = \frac{V_1 - V_2}{t} \qquad (4.26)$$

Although the distance between P_1 and P_2 was 2.5 times the thickness of the adhesive layer, because the Young's modulus of the adherend was more than 100 times that of the adhesive layer, the deformation of the adherend was negligibly small, and the relative displacement between P_1 and P_2 could be considered the relative displacement between the upper and lower interfaces of the adhesive layer. Therefore, in Eq. 4.26, the deformation of the adherends is ignored when calculating the strain in the adhesive layer.

The stress was calculated by dividing the tensile load by the cross-sectional area of the bonded joint.

The black curve in Fig. 4.13 shows the experimental stress–strain curve of the adhesive layer of the butt joint. As shown in this figure, compared with the stress–strain curves of the bulk adhesive specimen and TAST specimens shown in Fig. 4.6, the fracture strain of the butt joint was smaller than that of the bulk adhesive or TAST specimens, and the slope of the stress–strain curve after yielding was larger than that of the bulk adhesive or TAST specimens.

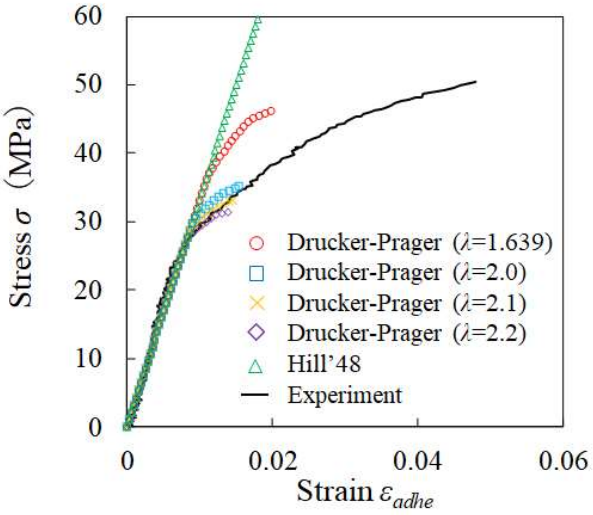

Fig. 4.13 Comparison between simulation results and experimental data for butt joint.

4.7.2 Comparison of experimental and simulated stress–strain curves

The method for simulating the stress–strain curve of the adhesive layer of the butt joint is described in this section. Figure 4.14 shows the boundary conditions of the butt joint. The butt joint specimen was modeled using plane-strain four-node quadrilateral elements (CPE4, ABAQUS). The adhesive elements used were 0.02 mm. It was well known that stress distribution in butt-joint was uniform except near the edge. Further subdivision of the mesh was not necessary since the analysis aim to evaluate uniform stress distribution at the center of the adhesive layer. The FEA was performed using a one-quarter model. The displacements in the X and Y directions on the left and bottom sides were constrained by symmetrical boundary conditions. The load was applied to the top nodes of the specimen with controlled displacement. The mechanical properties of the adherends were the same as those of the TAST specimens. The adhesive layer of the

butt joint was modeled using the exponent Drucker–Prager and Hill'48 models, and the material properties used are listed in Tables 4.2 and 4.3. However, for the value of the parameter λ in Table 4.2, not only 1.639 shown in the table but also several larger values were used in the FEA to discuss the effect of the hydrostatic stress.

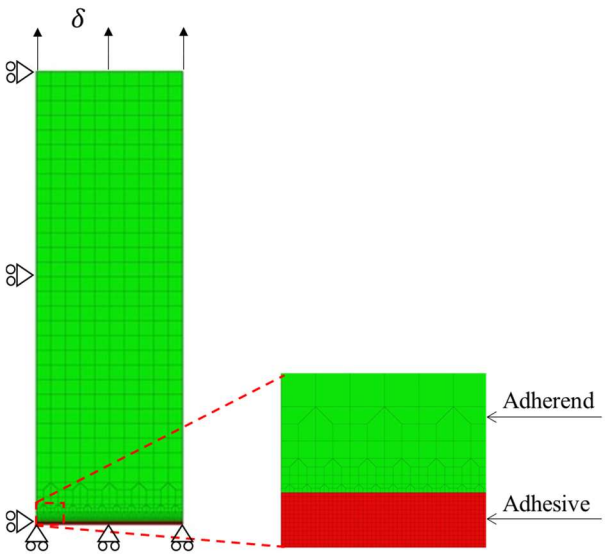

Fig. 4.14 Boundary conditions for butt joint.

The estimated stress–strain curves of the adhesive layer, in which the exponent Drucker–Prager and Hill'48 models were applied, are superimposed on the experimental curve in Fig. 4.13 using colored plots. The analysis curves with Drucker-Prager model were only available for the strain range of the plots, because iterative solution of nonlinear analysis was not converged above the plots. When the Drucker-Prager yield condition is applied to butt joints, it is inferred that the yield stress is excessively lower than in the analysis with the yield condition assuming iso-volumetric changes, due to the expansion stress acting on the adhesive layer. This would have made convergence of the residual forces difficult, resulting in divergence of the solution, and the FEA estimation curve would have been obtained only to a lower strain than the experimental curve. The stress–strain curve calculated using the Hill'48 model significantly overestimated the experimental curve. This significant discrepancy was caused by the fact that despite the large expansion stress acting on the adhesive layer of the butt joint under tensile loading, the Hill'48 model only considers the anisotropy of yielding under tension and shear loadings but does not consider the effect of hydrostatic stress.

The adhesive used in this experiment was a rubber-modified epoxy adhesive, and it is well known that when the expansion stress acts on the adhesive layer, the rubber

particles dispersed in the adhesive become voided, and the multiaxial stress state is relieved [20-22]. This also indicates that the effect of hydrostatic stress must be considered when estimating yielding behavior.

For the exponent Drucker–Prager model, the hydrostatic stress-sensitivity parameter λ is not only the ratio of shear yield stress to tensile yield stress but also affects the sensitivity of hydrostatic stress to the yield behavior. As shown in Fig. 4.13, the estimated stress with $\lambda = 1.639$, which could reproduce the yield stresses under tensile and shear loading conditions, overestimated the experimental stresses by approximately 30%. The figure shows that the estimated curve at $\lambda = 2.1$ was the most asymptotic to the experimental curve. These results showed that λ that could reproduce the experimental stress–strain curve was affected by the stress multiaxiality. In conventional analysis, λ is treated as a constant value. However, the results presented above indicated that λ was affected by the stress multiaxiality of the adhesive layer.

Generally, the parameter H, shown in Eq. 4.27, is used to indicate the stress multiaxiality.

$$H = \frac{\sigma_m}{\sigma_e} \qquad (4.27)$$

Here, σ_m and σ_e are the hydrostatic component and effective von Mises stress, in the elastic region, respectively. The effect of H on λ is shown in Fig. 4.15, where λ is the value that reproduced the stress–strain curves of the bulk specimen, TAST specimen, and butt joint, and H is the corresponding stress multiaxiality parameter of these specimens. This figure shows that λ was constant below $H = 1/3$ but increased when approaching to $H = 3$ in this study. In most studies on the estimation of stress–strain curves with the exponent Drucker–Prager model for adhesives, λ, which was fitted to the experimental stress–strain curves, was obtained from tensile and shear tests. Only Dean et al. [7] estimated λ fitted to experimental stress–strain curve of the butt joint and their result showed that λ was constant and independent of H, as indicated by open circles in Fig. 4.15. Because very few studies on the determination of λ in highly multiaxial stress conditions have been conducted, the relationship between λ and H is not clear. However, note that λ is not always constant but possibly increases when H in the adhesive layer becomes considerably high, as observed in this study. For adhesive joints with high stress multiaxiality in the adhesive layer, such as butt joints, the estimated stress using λ fitted under low stress multiaxiality conditions may be higher than the actual stress, depending on the type of adhesive.

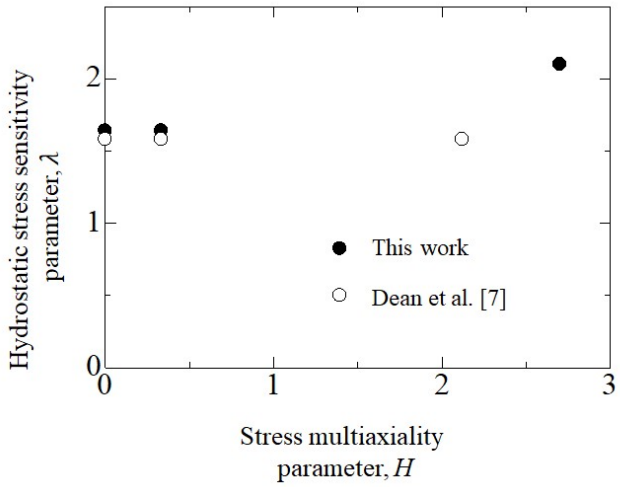

Fig. 4.15 Effect of stress multiaxiality parameter on hydrostatic stress sensitivity parameter.

4.8 Conclusions

An elastic–plastic model of adhesives applicable to a wide range of stress multiaxialities was explored for the film adhesive AF163-2U. The main conclusions are as follows:

1. The exponent Drucker–Prager and Hill'48 models were selected as elastic–plastic models applicable to low-stress multiaxial conditions. Subsequently, the parameters for these models were determined to fit the experimental yield stresses under tensile and shear loading conditions, where bulk adhesive specimens and TAST specimens were used. The hydrostatic stress sensitivity parameter for the exponent Drucker–Prager model was determined based on the plastic-work conjugate concept under tensile and shear loading conditions.
2. A tensile test of the adhesively bonded butt joint was conducted to obtain the stress–strain curves of the adhesive layer under high-stress multiaxiality conditions. In this experiment, the strain of the adhesive layer was calculated based on the relative displacement between two points on the adherend in the vicinity of the adhesive layer using DIC.
3. The obtained experimental stress–strain curve of the butt joints was compared with the estimated curves based on the exponent Drucker–Prager and Hill'48 models. As a result, the estimated stresses from Hill'48 model significantly overestimated the experimental stresses. For the exponent Drucker–Prager model, the estimated stress

with $\lambda = 1.639$, which could reproduce the yield stresses under tensile and shear loading conditions, overestimated the experimental stresses by approximately 30%, whereas the stress estimated with $\lambda = 2.1$ was in close agreement with the experimental stresses. Thus, it was confirmed that λ fitted to the experimental stress is not always constant but increases with the stress multiaxiality in the adhesive layer.

References

[1] Crocker LE, Duncan BC, Hughes RG, Urquhart JM. Hyperelastic modelling of flexible adhesives. UK: Materials Centre. National Physical Laboratory; 1999.

[2] Duncan B. The hyperelastic properties of a polyurethane adhesive. UK: Materials Centre. National Physical Laboratory; 2001.

[3] Pearson I, Pickering M. The determination of a highly elastic adhesive's material properties and their representation in finite element analysis. Finite Elem Anal Des. 2001;37:221-232. https://doi.org/10.1016/S0168-874X(00)00031-7

[4] Ameli A, Azari S, Papini M, Spelt JK. Crack path selection in the fracture of fresh and degraded epoxy adhesive joints. Eng Frac Mech. 2011;78:1986-2003. https://doi.org/10.1016/j.engfracmech.2011.03.020

[5] Azari S, Papini M, Spelt JK. Effect of adhesive thickness on fatigue and fracture of toughened epoxy joints - Part II: Analysis and finite element modeling. Eng Frac Mech. 2011;78:138-152. https://doi.org/10.1016/j.engfracmech.2010.07.006

[6] Chun HW, Peter C. Plastic yielding of a fillm adhesive under multiaxial stresses. Int J Adhes Adhes. 2000;20:155-164. https://doi.org/10.1016/S0143-7496(99)00033-0

[7] Dean G, Crocker L, Read B, Wright L. Prediction of deformation and failure of rubber-toughened adhesive joints. Int J Adhes Adhes. 2004;24:295-306. https://doi.org/10.1016/j.ijadhadh.2003.08.002

[8] Garcı´a JA, Chiminelli A, Garcı´a B, Lizaranzu M, Jiménez MA. Characterization and material model definition of toughened adhesives for finite element analysis. Int J Adhe Adhes. 2011;31:182-192. https://doi.org/10.1016/j.ijadhadh.2010.12.006

[9] Chiminelli A, Breto R, Jiménez MA, Velasco F, Abenojar J, Martínez MA. Experimental method for the determination of material parameters of plasticity models for toughened adhesives. Int J Adhes Adhes. 2016;68:182-187. https://doi.org/10.1016/j.ijadhadh.2016.03.004

[10] Quan H, Alderliesten R. On the effect of plastic model on simulation of adhesive bonded joints with FM94. Int J Adhes Adhes. 2021;110:102916. https://doi.org/10.1016/j.ijadhadh.2021.102916

[11] Hill R. A theory of the yielding and plastic flow of anisotropic metals. Proc R Soc. 1948, 193(1033):281-297.
[12] Barlat, F., Brem, J. C., Yoon, J.W., Chung, K., Dick, R.E., Lege, D.J., Pourgoghrat, F., Choi, S.H., Chu, E., 2003. Plane stress yield function for aluminum alloy sheets – Prat 1: theory. International Journal of Plasticity 19, 1297-1319. https://doi.org/10.1016/S0749-6419(02)00019-0
[13] Yoshida, F., Hamaski, H., Uemori, T., 2013. A user-friendly 3D yield function to describe anisotropy of steel sheets, International Journal of Plasticity 45, 119-139. https://doi.org/10.1016/j.ijplas.2013.01.010
[14] Soare, S.C., 2023. Bezier5YS and SHYqp: A general framework for generating data and modeling symmetric and asymmetric orthotropic yield surfaces. European Journal of Mechanics A Solids 97, 104781. https://doi.org/10.1016/j.euromechsol.2022.104781
[15] Kosmann J, Völkerink O, Schollerer MJ, Holzhüter D, Hühne C. Digital image correlation strain measurement of thick adherend shear test specimen joined with an epoxy film adhesives. Int J Adhes Adhes. 2019;90:32-37. https://doi.org/10.1016/j.ijadhadh.2019.01.024
[16] ASTM D 5656-04 (2004). Standard test method for thick-adherend metal lap-shear joints determination of the stress-strain behavior of adhesives in shear by tension loading. ASTM standards.
[17] SIMULIA user assistance, Dassault Systems 2021.
[18] Yoshida, F., Hamaski, H., Uemori, T., 2015. Modeling of anisotropic hardening of sheet metals including description of the Bauschinger effect, International Journal of Plasticity 45, 119-139. https://doi.org/10.1016/j.ijplas.2015.02.004
[19] Adams R, Comyn J, Wake WC. Structural adhesive joints in engineering, second edition, Chapman & Hall (1997).
[20] Kinloch AJ, Shaw SJ, Tod DA, Hunston DL. Deformation and fracture behavior of a rubber toughened epoxy: 1. Microstructure and fracture studies. Polymer. 1983; 24:1341-1354. https://doi.org/10.1016/0032-3861(83)90070-8
[21] Kinloch AJ, Shaw SJ, Hunston DL. Deformation and fracture behavior of a rubber toughened epoxy: 2. Failure criteria. Polymer. 1983;24:1355-1363. https://doi.org/10.1016/0032-3861(83)90071-X
[22] Yee AF, Pearson RA. Toughening mechanisms in elastomer-modified epoxies. part 1 Mechanical studies. J Mater Sci. 1986;21:2462-2474. https://doi.org/10.1007/BF01114293

Chapter 5 Conclusions

5.1 Summaries of this thesis

The purpose of this study was to assess the experimental methods and finite element simulation methods for predicting the strength of toughened epoxy adhesive joints. In order to investigate the influence of the fracture toughness of adhesively bonded joints on the accuracy of FE simulation, the experimental test and their fracture behavior under the mixed-mode conditions were evaluated and validated. The effect of hydrostatic stress on yield stress in the multiaxial stress field in the adhesive joints was also evaluated and verified. As a result, the following findings were obtained.

In chapter 2, fracture toughness tests using toughened epoxy adhesive joints were conducted to obtain *R*-curves under the various mixed mode conditions. It was clarified that complicated crack propagation path of the fracture surface of the toughened adhesive joint affects the mechanism of the *R*-curve characteristic in Mode II dominant region of energy release rate in the mixed-mode conditions. The *R*-curves found that the total energy release rate G_T was almost constant irrespective of crack length in Mode I dominant region, whereas in Mode II dominant region, G_T increased up to crack length reaches approximately 10 mm, after that, it remains at constant value.

In chapter 3, CZM simulations of fracture toughness tests under the various mixed mode conditions were performed using trapezoidal traction–separation law. The failure criteria were employed linear and power-law type models. CZM parameters of G_{IC} and G_{IIC} were defined as the energy release rate in the plateau region of *R*-curve. The simulation results found that a power-law fracture model with $n = 1.8$ which determined by experimental results was suitable and reproduced the peak load of the experimental load–displacement curves.

In chapter 4, the stress–strain curves were evaluated for butt joint tensile tests with high stress-multiaxiality by using exponential Drager-Prager model which could define hydrostatic stress sensitivity. The exponential Drucker Prager model could reproduce the yield stresses for butt-joint tensile tests by adjusting the hydrostatic stress sensitivity parameter λ. The exponential Drucker–Prager model with $\lambda = 1.639$ which was defined under tensile and shear loading conditions overestimated the yield stress of butt joint tensile test. This result showed that λ is not always constant and should be set an appropriate value depending on the stress multiaxiality parameter H in the adhesive layer.

A series of this studies have found that *R*-curves under the mixed mode conditions is crucial for toughened epoxy adhesive joints. The *R*-curve characteristic in the mixed mode conditions would contribute in improving the accuracy of CZM analysis. In the

case of stress analysis for butt joints, which are subject to high hydrostatic stress, it is clear that setting the appropriate hydrostatic stress sensitivity parameter could improve the accuracy of the analysis.

5.2 Expected outcomes and future work

Since modern adhesives are highly specialized, it is critical that selecting the proper one for specific needs. The consideration of the adhesive from among many adhesives that suits the applications has delayed the design development, because it takes a lot of time and costs. In this respect, if the *R*-curve could be used as one of the alternative options to select the best adhesive, it will contribute to improving the efficiency of designing adhesive structures.

Generally, adhesive selection has been determined by an adhesive expert based on experience, prior knowledge and trial and error. Adequate simulation tools to support adhesive bonding in the design processes is lacking in the R&D department of a company. In that context, the proposal of the crack propagation analysis for the peak load of the adhesive joints may contribute to simple and accurate strength prediction of the mechanical design in modern industry.

To prevent adhesive failure, the reliability of stress analysis for adhesively bonded joint is crucial. Adhesive joints cause stress concentration at the edge. Therefore, more accurate method of estimating stress is needed. The evaluation of the yield conditions and plastic behavior of toughened epoxy adhesive at different stress multiaxialities could contribute to improving the accuracy of stress evaluation of adhesive joints.

This study is only basic research on the fracture toughness and material yield conditions for toughened epoxy adhesive. There are some issues that should be considered in the future. The evaluation of the damage length at stress whitening region in the crack tip is just a simple evaluation of the external observation, so more detail internal microscopic fracture mechanism is needed. The peak load predicted by CZM was not only determined by the energy-based failure criterion but was affected by other parameters. Therefore, it is necessary to investigate how CZM parameters should be determine more appropriate. The stress multiaxialities is not uniform in actual bonded joints. It is necessary to develop a calculation system that selects alternative hydrostatic stress sensitivity parameters according to the stress multiaxialities.

Further research is needed to resolve the remaining issues.

Acknowledgments

I have received a lot of help and guidance from many people during my doctoral studies. I would like to express my sincere gratitude to all the people who have helped me.

First of all, I would like to express my sincere gratitude to the four members of this study. I am deeply appreciative of Professor Makoto Imanaka for his tremendous support in this study including guidance of experimental tests, supervised and provided suggestions for my experiments and giving me this good opportunity. When I was helpless and difficult to continue my research, he gave me a lot of help and overcame the difficulties. Without his enlightened guidance, impressive kindness, I would not have been able to complete this study. Associate Professor Ryutaro Hino gave me the reasonable guidance of DIC analysis and led me data analysis scheme. When we started this study in April 2021, we struggled with the experimental testing that had stalled us by COVID-19 state of emergency declaration. In this situation, he quickly resolved this problem through detailed discussions and careful preparation, and he taught me how important it is to collaborate with researchers from different fields. Professor Masaki Omiya helped me technical support for FE analysis for CZM and *J*-integral method. He responded very quickly and accurately to our analysis and provided precise guidance on how to improve the calculations. Professor Fusahito Yoshida supervised and provided us very important issues about elastic-plastic analysis and taught me the importance of originality, which is the heart of the study. I will never forget the time I spent with these four professors.

I also thank Dr. Yusuke Fukuchi (New Industry Research Organization) for designing and drawing the mixed-mode fracture toughness test jig. I am also greatly indebted to Associate Professor Keisuke Hara (National Institute of Technology Wakayama College) who provided experimental guidance for adhesively bonded joints and technical support for fracture toughness tests. And I would like to thank my fellow the staff of Hiroshima prefecture for their understanding and support of this research.

Then, my thanks are extended to the past and present students of Engineering Elasto-Plasticity Laboratory, in Department of Mechanical Science and Engineering, Hiroshima University, for their enthusiastic help to me. Matsugi Kouki helped me significantly with my experiments and encouraged my Ph.D. student life. Kohei Iwanaga and Atsushi Tsuchiya helped me with experimental tests related to DIC analysis.

Finally, I would like to express my heartfelt gratitude to my family have been always supporting to me.

Published papers in regard to this thesis

[1] Kouno Y, Imanaka M, Hino R, Omiya M, Yoshida F, *R*-curve behavior of adhesively bonded composite joints with highly toughened epoxy adhesive under mixed mode conditions. Int. J. Adhes. Adhes. 2021:105,102762.
https://doi.org/10.1016/j.ijadhadh.2020.102762

[2] Kouno Y, Imanaka M, Hino R, Omiya M, Yoshida F, Estimation of fracture behavior of CFRP/CFRP adhesively bonded joints under mixed-mode conditions using a cohesive zone model. J Adhes Sci Technol. 2024:1-18.
https://doi.org/10.1080/01694243.2024.2348244

[3] Kouno Y, Imanaka M, Hino R, Omiya M, Yoshida F, Plastic behavior of a film type of epoxy adhesive under a wide range of stress multiaxiality conditions. J Adhes Sci Technol. 2024:1-20.
https://doi.org/10.1080/01694243.2024.2326708